J. Fluid Mech. (2014), *vol.* 747, *pp.* 288–315.
doi:10.1017/jfm.2014.157

Transport equation for the mean turbulent energy dissipation rate in low-R_λ grid turbulence

L. Djenidi† and R. A. Antonia

Discipline of Mechanical Engineering, School of Engineering, University of Newcastle, Newcastle, 2308 NSW, Australia

(Received 14 November 2013; revised 18 March 2014; accepted 18 March 2014; first published online 17 April 2014)

A direct numerical simulation (DNS) based on the lattice Boltzmann method (LBM) is carried out in low-Reynolds-number grid turbulence to analyse the mean turbulent kinetic energy dissipation rate, $\overline{\epsilon}$, and its transport equation during decay. All the components of $\overline{\epsilon}$ and its transport equation terms are computed, providing for the first time the opportunity to assess the contribution of each term to the decay. The results indicate that although small departures from isotropy are observed in the components of $\overline{\epsilon}$ and its destruction term, there is sufficient compensation among the components for these two quantities to satisfy isotropy to a close approximation. A short distance downstream of the grid, the transport equation of $\overline{\epsilon}$ simplifies to its high-Reynolds-number homogeneous and isotropic form. The decay rate of $\overline{\epsilon}$ is governed by the imbalance between the production due to vortex stretching and the destruction caused by the action of viscosity, the latter becoming larger than the former as the distance from the grid increases. This imbalance, which is not constant during the decay as argued by Batchelor & Townsend (*Proc. R. Soc. Lond.* A, vol. 190, 1947, pp. 534–550), varies according to a power law of x, the distance downstream of the grid. The non-constancy implies a lack of dynamical similarity in the mechanisms controlling the transport of $\overline{\epsilon}$. This is consistent with the fact that the power-law-decay ($\overline{q^2} \sim x^n$) exponent n is not equal to -1. It is actually close to -1.6, a value in keeping with the relatively low Reynolds number of the simulation. These results highlight the importance of the imbalance in establishing the value of n. The $\overline{\epsilon}$-transport equation is also analysed in relation to the power-law decay. The results show that the power-law exponent n is controlled by the imbalance between production and destruction. Further, a relatively straightforward analysis provides information on the behaviour of n during the entire decay process and an interesting theoretical result, which is yet to be confirmed, when $R_\lambda \to 0$, namely, the destruction coefficient G is constant and its value must lie between 15/7 and 30/7. These two limits encompass the predictions for the final period of decay by Batchelor & Townsend (1947) and Saffman (*J. Fluid Mech.*, vol. 27, 1967, pp. 581–593).

Key words: homogeneous, isotropic turbulence, turbulence simulation

† Email address for correspondence: lyazid.djenidi@newcastle.edu.au

1. Introduction

The mean turbulent kinetic energy dissipation rate, $\overline{\epsilon}$, defined as

$$\overline{\epsilon} = \frac{\nu}{2}\overline{\left(\frac{\partial u_i}{\partial x_j} + \frac{\partial u_j}{\partial x_i}\right)^2} \quad (i, j = 1, 2, 3) \tag{1.1}$$

where ν is the fluid kinematic viscosity, u_i are the velocity fluctuations in the x_i directions (the overbar denotes ensemble averaging), is of fundamental interest in freely decaying turbulence because it determines the rate at which the turbulence decays. Also of importance is its transport equation, which remains the most uncertain part of turbulence modelling. The equation plays a vital role in the study of small-scale turbulence, although under a simpler form, which, for high-Reynolds-number homogeneous turbulence, where $\overline{\epsilon} = \nu\overline{\omega_i\omega_i}$ (ω_i are the fluctuating vorticity components and $\overline{\omega_i\omega_i}$ is the mean enstrophy), is

$$\frac{\mathrm{d}\overline{\epsilon}}{\mathrm{d}t} = 2\nu\overline{\left(\omega_i\omega_j\frac{\partial u_i}{\partial x_j}\right)} - 2\nu^2\overline{\left(\frac{\partial \omega_i}{\partial x_j}\right)\left(\frac{\partial \omega_i}{\partial x_j}\right)}, \tag{1.2}$$

with

$$\frac{\mathrm{d}\overline{\epsilon}}{\mathrm{d}t} = \frac{\partial\overline{\epsilon}}{\partial t} + \overline{U_k}\frac{\partial\overline{\epsilon}}{\partial x_k}. \tag{1.3}$$

The equation shows that for homogeneous turbulence, $\overline{\epsilon}$ is governed by the difference between the production due to the stretching of vorticity and its destruction through the action of viscosity (the first and second terms, respectively, on the right of (1.2), first established by von Kármán (1937) and subsequently analysed in the context of decaying grid turbulence by Batchelor & Townsend (1947), hereafter denoted BT47. This equation is derived by writing the transport equation for $\overline{\omega_i\omega_i}$ using homogeneity, multiplying it by ν, and neglecting the turbulent and viscous diffusions of vorticity. It plays a critical role in various turbulence models used in computational fluid dynamics (CFD). For example, Hanjalic & Launder (1972) proposed closure approximations for the different terms of the equation, in particular, the sum of the production and destruction terms. Arguing that, at a sufficiently large Reynolds number, this sum is controlled by the dynamics of the energy cascade process transporting energy from low to high wavenumbers and is thus independent of viscosity, the sum was modelled as $C_{\epsilon 2}\overline{\epsilon}/\overline{q^2}$, where $\overline{q^2}$ is the mean turbulent kinetic energy and $C_{\epsilon 2}$ a constant. The final form of the modelled equation is

$$\frac{\mathrm{d}\overline{\epsilon}}{\mathrm{d}t} = \frac{\overline{\epsilon}}{\overline{q^2}}(C_{\epsilon 1}P - C_{\epsilon 2}\overline{\epsilon}) \tag{1.4}$$

where $C_{\epsilon 1}$ is a constant and P is the turbulence production. The constants $C_{\epsilon 1}$ and $C_{\epsilon 2}$, which are supposed to be universal, were established using data from near-wall turbulent flows and decaying grid turbulence, respectively. It is now generally accepted that these constants are flow dependent. Rubinstein & Clark (2005) argued that no single $\overline{\epsilon}$ equation can be consistent with all classes of turbulent flows (at least when $C_{\epsilon 1}$ and $C_{\epsilon 2}$ are considered constant). Equally of interest in CFD are the possible variations of these constants with the Reynolds number. This is particularly important for low-Reynolds-number turbulence modelling.

While (1.2) is important in the study of turbulence from both modelling and theoretical points of view, it is nevertheless only a simplified form of the actual transport equation for $\overline{\epsilon}$ (Chassaing 2000):

$$\begin{aligned}
\frac{\partial \overline{\epsilon}}{\partial t}+\overline{U_k}\frac{\partial \overline{\epsilon}}{\partial x_k} = & -\nu\overline{\left(\frac{\partial u_i}{\partial x_j}+\frac{\partial u_j}{\partial x_i}\right)u_k}\frac{\partial}{\partial x_k}\left(\frac{\partial \overline{U_i}}{\partial x_j}+\frac{\partial \overline{U_j}}{\partial x_i}\right) && T_{1a}\\
& -\nu\left[\overline{\left(\frac{\partial u_i}{\partial x_j}+\frac{\partial u_j}{\partial x_i}\right)\frac{\partial u_k}{\partial x_j}}\frac{\partial \overline{U_i}}{\partial x_k}+\overline{\left(\frac{\partial u_i}{\partial x_j}+\frac{\partial u_j}{\partial x_i}\right)\frac{\partial u_k}{\partial x_i}}\frac{\partial \overline{U_j}}{\partial x_k}\right] && T_{1b}\\
& -\nu\left[\overline{\left(\frac{\partial u_i}{\partial x_j}+\frac{\partial u_j}{\partial x_i}\right)\frac{\partial u_i}{\partial x_k}}\frac{\partial \overline{U_k}}{\partial x_j}+\overline{\left(\frac{\partial u_i}{\partial x_j}+\frac{\partial u_j}{\partial xi}\right)\frac{\partial u_j}{\partial x_k}}\frac{\partial \overline{U_k}}{\partial x_i}\right] && T_{1c}\\
& -\nu\overline{\left(\frac{\partial u_i}{\partial x_j}+\frac{\partial u_j}{\partial x_i}\right)\left(\frac{\partial u_i}{\partial x_k}\frac{\partial u_k}{\partial x_j}+\frac{\partial u_j}{\partial x_k}\frac{\partial u_k}{\partial x_i}\right)} && T_2\\
& -\frac{\partial \overline{\epsilon u_k}}{\partial x_k} && T_3\\
& -\frac{2\nu}{\rho}\overline{\left(\frac{\partial u_i}{\partial x_j}+\frac{\partial u_j}{\partial x_i}\right)\frac{\partial^2 p}{\partial x_i \partial x_j}} && T_4\\
& +\nu\frac{\partial^2 \overline{\epsilon}}{\partial x_k \partial x_k} && T_5\\
& -\nu^2\overline{\left[\frac{\partial}{\partial x_k}\left(\frac{\partial u_i}{\partial x_j}+\frac{\partial u_j}{\partial x_i}\right)\right]^2} && T_6. \quad (1.5)
\end{aligned}$$

Collectively, terms T_{1a}, T_{1b}, and T_{1c} on the right of the equation represent the production of the dissipation rate by interaction between the mean flow and the turbulence. Term T_2 is the production of the dissipation rate by turbulent stretching (or creation). Term T_3 represents the diffusion of the dissipation rate by the turbulence. Term T_4 is the dissipation rate/pressure gradient correlation. Term T_5 is the viscous diffusion, and term T_6 is the destruction of the dissipation rate (or destruction by viscosity). It is evident that measuring all the terms of this equation represents an almost insurmountable task for experimentalists. At present, access to all these terms can be achieved only through a direct numerical simulation (DNS). Mansour, Kim & Moin (1987) used their DNS database of a fully developed turbulent channel flow to compute all the terms on the right-hand side of the equation for the pseudo-dissipation rate,

$$\overline{\varepsilon}=\nu\overline{\frac{\partial u_i}{\partial x_k}\frac{\partial u_i}{\partial x_k}}=\overline{\epsilon}-\frac{\partial}{\partial x_k}\left(\nu\overline{u_i\frac{\partial u_k}{\partial x_i}}\right) \quad (1.6)$$

(for incompressible flow), which is relatively simpler than (1.5) (Chassaing 2000). Following Corrsin (1953), Bradshaw & Perot (1993) showed that the difference between $\overline{\varepsilon}$ and $\overline{\epsilon}$ is less than 2 % in the viscous wall region, and negligible elsewhere. Thus, in practice, it is often common to ignore the difference between $\overline{\varepsilon}$ and $\overline{\epsilon}$.

Since it is virtually impossible to measure all the terms in (1.5), much attention has been paid to (1.2), mostly in decaying grid turbulence, as this flow represents a good approximation of homogeneous isotropic turbulence (HIT). For this flow, (1.2) becomes (e.g. Zhou *et al.* 2000)

$$\frac{\mathrm{d}\overline{\epsilon}}{\mathrm{d}t}=\frac{7\overline{\epsilon}^{3/2}}{3(15)^{1/2}\nu^{1/2}}\left(S-\frac{2G}{R_\lambda}\right) \quad (1.7)$$

where the destruction coefficient G (sometimes called palinstrophy coefficient) is defined as

$$G = \overline{u^2}\frac{\overline{\left(\partial^2 u/\partial x^2\right)^2}}{\left[\overline{(\partial u/\partial x)^2}\right]^2} \tag{1.8}$$

and the skewness S of the velocity derivative is given by

$$S = -\frac{\overline{(\partial u/\partial x)^3}}{\left[\overline{(\partial u/\partial x)^2}\right]^{3/2}}, \tag{1.9}$$

with $R_\lambda = u'\lambda/\nu$ the Taylor microscale Reynolds number; a prime denotes the root-mean-square (r.m.s.) value and λ is the Taylor microscale ($\lambda^2 = \overline{u^2}/\overline{(\partial u/\partial x)^2}$). If turbulence decays according to a power law, $\overline{q^2} \sim x^n$ ($\overline{q^2}$ is the mean turbulent energy, x the distance downstream of the grid and $n < 0$) then $\overline{\epsilon} \sim nx^{n-1}$ and (1.7) can be simplified to the form (George 1992; Zhou *et al.* 2000)

$$G = \frac{15}{7}\left(\frac{n-1}{n}\right) + \frac{SR_\lambda}{2}. \tag{1.10}$$

Equation (1.10) reduces to that obtained by BT (1947; 1948*a*) when $n = -1$, which corresponds to the asymptotic state of decay at very large Reynolds numbers (e.g. Dryden 1943; Speziale & Bernard 1992). Using a single hot wire, BT47 measured S and G at several locations downstream of their grid. Their results show that S and G are approximately constant while R_λ has a general tendency to decrease, albeit slightly, with x/M, where M is mesh size. Antonia, Zhou & Zhu (1998) used three-component vorticity measurements in grid turbulence and showed that both (1.2) and (1.10) were satisfied reasonably well. However, while their data indicate that S is approximately constant with respect to x/M, G and R_λ decrease slowly with x/M. This is also seen in the data of Antonia *et al.* (2002). Further, Lee *et al.* (2014) showed that the ratio G/R_λ increases while the product SR_λ decreases. Constancy of SR_λ requires that either S and R_λ are both constant or $S \sim R_\lambda^{-1}$. The first condition appears to be only approximately satisfied by the data of BT47 for $R_M = 5620$. The second, which is a consequence of George's equilibrium similarity theory (George 1992), has yet to be verified. It is also of interest to point out that the limiting behaviour of S as R_λ approaches zero (i.e. the final stage of the decay) remains an open issue (e.g. Batchelor & Townsend 1948*a*; Reid 1956; Ling & Huang 1970; Bennett & Corrsin 1978; Tavoularis, Bennett & Corrsin 1978).

Equations (1.2), (1.4), (1.7) and (1.10) are assumed to be valid at very high Reynolds numbers and for homogeneous and/or isotropic conditions. To date, their validation (in particular (1.7) and (1.10) which have been used for low-Reynolds-number turbulence flows) has not been thoroughly investigated, mainly because of the difficulties of measuring all the terms of (1.5). Even in the case of grid turbulence, which plays a pivotal role in the theory of turbulence, such validation is lacking. Quite remarkably, there has been so far no attempt to test these equations through DNS. Thus, the purpose of this work is to examine (1.5) in the context of decaying grid turbulence, and compare it with (1.2) and (1.7). All terms of (1.2), (1.5), and (1.7) except T_{1a}, T_{1b} and T_{1c}, are directly computed through DNS which is carried out via the lattice Boltzmann method (LBM). There is currently no reported experimental

or numerical data corresponding to all these terms in these equations. We believe that the study provides the first detailed results on how these transport equations evolve through the generation of turbulence and its subsequent decay at low Reynolds number. It thus contributes to the study of low-Reynolds-number turbulence, a subject which is yet to be fully investigated and, not surprisingly, inadequately understood.

2. Numerical procedure

2.1. *Lattice Boltzmann method*

A DNS is carried out using the LBM. Rather than solving the governing fluid equations (Navier–Stokes equations), the LBM solves the Boltzmann equation on a lattice (Frisch, Hasslacher & Pomeau 1986). The method has been successfully used to simulate turbulent flows (Burattini *et al.* 2006; Djenidi 2006, 2008). Note that unless otherwise specified all quantities are either expressed in lattice units or made non-dimensional. Details on the LBM can be found in Chen & Doolen (1998) or Succi (2001). Implementation of the LBM for this flow is given in Djenidi (2006) and Djenidi, Tardu & Antonia (2013*a*).

2.2. *Computational domain and boundary conditions*

The computational uniform Cartesian mesh consists of $1600 \times 240 \times 240$ mesh points with $\Delta x = \Delta y = \Delta z = 1$ (x is the longitudinal direction and y and z the lateral directions). The turbulence-generating grid is made up of 6×6 floating flat square elements in an aligned arrangement (see Djenidi *et al.* 2013*a*). Each element is represented by $1 \times 20 \times 20$ mesh points and the mesh spacing (M) between the centre of two elements is 40 mesh points (i.e. $2D$, D being the length of an element side), yielding a grid solidity of 0.25. The downstream distance extends to $x/D = 70$ (equivalently $x/M = 35$), where the origin of x is the grid plane and $D = 20$ mesh points is the grid-element side length. Note that the same distance would require far too large a number of mesh points if a grid made of vertical and horizontal bars and with the same solidity were to be used. This is the main reason why the square elements were chosen.

Periodic conditions are applied in the y- and z-directions. At the inlet, a uniform velocity ($U_0 = 0.05$, and $V_0 = W_0 = 0$) is imposed, and a convective boundary condition is applied at the outlet. It was observed that the convective condition affected marginally the simulation results within a distance of less than $2D$ upstream of the outlet. A no-slip condition at the grid elements is implemented with a bounce-back scheme (Succi 2001). The Reynolds number, R_M, is approximately 3200. This is a relatively small value, which allows a reasonably good grid resolution which varies from approximately 2.9η at $x/D = 8$ to 0.78η at $x/D = 68$; η is the Kolmogorov length scale. A check for the computational accuracy is provided in the Appendix Although a steady-state solution is obtained after 10 000 iterations, the first velocity field is saved after the 50 000th iteration. Subsequently, 40 velocity fields are recorded, each separated by approximately 15 000 iterations (approximately $5\lambda/u'$, u' being the velocity fluctuation r.m.s. at $x/D = 30$) to ensure that two consecutive fields are uncorrelated. In order to avoid the occurrence of instabilities where the magnitude of the local strain rate could be large, mainly around the grid, a large-eddy simulation (LES) scheme with a filter size equal to the mesh resolution was introduced. The LES scheme is based on the Smagorinsky model and developed for the LBM by Hou *et al.* (1996); details can be found in Djenidi (2006) and Djenidi *et al.* (2013*a*).

R_M	x/D	$\Delta x/\eta$	$L/\Delta x$	R_λ
3200	8–68	2.9–0.78	8.5–27	56–19

TABLE 1. Variations of the ratios x/D, $\Delta x/\eta$, $L/\Delta x$ and R_λ.

The value of R_λ varies from approximately 60 at $x/D = 8$ to approximately 18 at $x/D = 70$. It should be noted that R_λ decreases rapidly from a maximum of approximately 1300 at $x/D = 0.5$ to 92 at $x/D = 5$. The rate at which it decreases is subsequently reduced. For example, $R_\lambda = 25$ at $x/D = 30$ and $R_\lambda = 19$ at $x/D = 65$. The strong initial drop in R_λ indicates a transient stage. Beyond that regime, R_λ is comparable to the values of BT47 ($R_\lambda \simeq 22$ for $20 \leqslant x/M \leqslant 120$) for $R_M = 5620$. Table 1 reports variations of some characteristic length scales with the distance downstream of the grid.

3. The mean turbulent energy dissipation rate $\overline{\epsilon}$

The streamwise variation of $\langle\epsilon\rangle$ is shown in figure 1; the symbol $\langle.\rangle$ represents time and space (in a plane perpendicular to the mean flow) averaging over 40 flow realizations. Djenidi *et al.* (2013*a*) showed that single-point temporally averaged statistics are equal to spatially averaged (over a transverse plane) statistics for one realization. They also showed that the flow is spatially homogeneous (in planes perpendicular to the mean flow) for $x/D \geqslant 10$. Thus, since the flow is stationary in time and spatially homogeneous in the transverse directions, and the temporal and spatial averages are equivalent, they concluded that the ergodic hypothesis is satisfied in planes perpendicular to the mean flow. This implies that the present time–space averaging is justified and $\langle\epsilon\rangle$ is equivalent to the ensemble-averaged value $\overline{\epsilon}$ in planes perpendicular to the mean flow for $x/D \geqslant 10$. Accordingly, the notations $\langle a\rangle$ and $\overline{a}$ will be used interchangeably. It is interesting to note that the results of Djenidi *et al.* (2013*a*) vindicate the justification for relaxing Corrsin's second and third criteria on homogeneity; these state that ratio L/M (L is the height/diameter of the wind tunnel) should be large and measurements should be made at least $40M$ downstream of the grid for the turbulence to be homogeneous in planes perpendicular to the main flow. These arguments were for a grid made of vertical and horizontal bars whose two-dimensional wakes interact to generate the turbulent field. These arguments are less likely to apply to the present grid made of floating flat square elements where individual three-dimensional wakes interact to generate the turbulent field.

Figure 1 also reports the streamwise variation of $\overline{\epsilon}_{hom} = \nu\overline{\omega_i\omega_i}$, the homogeneous value of $\overline{\epsilon}$, and $\overline{\epsilon}_{iso} = 15\nu\overline{(\partial u/\partial x)^2}$, the isotropic value of $\overline{\epsilon}$. The good agreement between $\overline{\epsilon}$ and $\overline{\epsilon}_{hom}$ confirms that the small-scale motion satisfies homogeneity closely, except immediately downstream of the grid. It is remarkable that there is such a close agreement between $\overline{\epsilon}$ and $\overline{\epsilon}_{hom}$ beyond a value of x/D as small as 0.5, and between $\overline{\epsilon}$ and $\overline{\epsilon}_{iso}$ when $x/D > 3$; $\overline{\epsilon}$, $\overline{\epsilon}_{iso}$ and $\overline{\epsilon}_{hom}$ become indistinguishable at $x/D = 3$. From a practical point of view, the figure suggests that $\overline{\epsilon}_{iso}$ can be used to estimate the true dissipation rate in grid turbulence, even at an early stage of the decay.

The equality between $\overline{\epsilon}$ and $\overline{\epsilon_{iso}}$ needs to be discussed as it does not necessarily imply that local isotropy is satisfied rigorously. Antonia *et al.* (1998) argued that there is in fact a compensating effect among the 12 components of $\overline{\epsilon}$. Figure 2 shows the streamwise distributions of all the terms of $\overline{\epsilon}$:

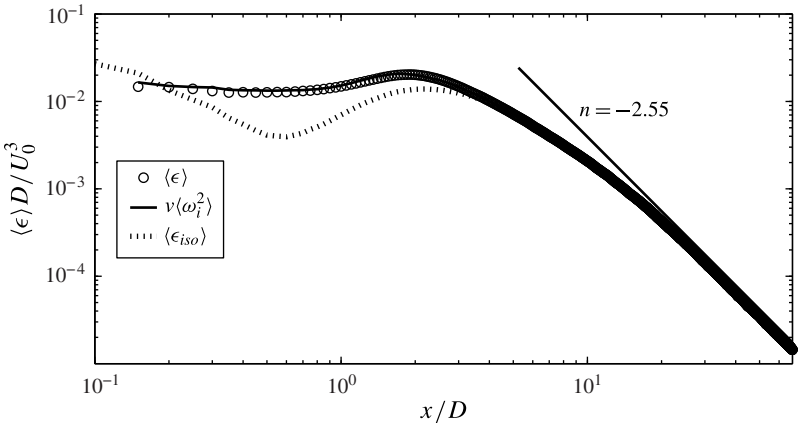

FIGURE 1. Streamwise variation of $\overline{\epsilon}D/U_0^3$ downstream of the grid. Also shown are the homogeneous and isotropic values of $\overline{\epsilon}$.

$$\overline{\epsilon} = \nu(2\overline{u_{1,1}^2} + 2\overline{u_{2,2}^2} + 2\overline{u_{3,3}^2} + \overline{u_{1,2}^2} + \overline{u_{2,1}^2} + \overline{u_{1,3}^2} + \overline{u_{3,1}^2} + \overline{u_{2,3}^2} + \overline{u_{3,2}^2} + 2\overline{u_{1,2}u_{2,1}} + 2\overline{u_{1,3}u_{3,1}} + 2\overline{u_{2,3}u_{3,2}}) \tag{3.1}$$

(with $u_{i,j} = \partial u_i/\partial x_j$; in the rest of the text we will use the following convention: $i, j, k = 1, 2, 3$, $1 \equiv x$, $2 \equiv y$, $3 \equiv z$, $u_1 = u$, $u_2 = v$, and $u_3 = w$). Clearly, all terms contribute to $\overline{\epsilon}$, with the first nine terms on the right-hand side of (3.1) (denoted $d1$–$d9$) positive and the three 'cross-derivative products' (denoted $d10$, $d11$, $d12$) negative. Note that lateral homogeneity implies $d2 = d3$, $d4 = d6$, $d5 = d7$, $d8 = d9$ and $d10 = d11$. If isotropy were satisfied then the ratios $di/d1$ ($i = 2,\ldots, 9$) should all be equal to 1 and $-di/d1$ ($i = 10, 11, 12$) be equal to 0.5. Although not shown here, these ratios are found to differ slightly from 1 and 0.5 throughout the decay. For example at $x/D = 25$, $d2/d1 = 1.03$, $d4/d1 = 0.98$, $d5/d1 = 0.96$, $d8/d1 = 0.97$, $-d10/d1 = 0.50$ and $-d12/d1 = 0.53$, indicating small departures from isotropy; for $d1$–$d9$, the maximum departure is approximately 3 % whereas it is almost 6 % for the cross-derivative terms ($d10$–$d12$), reflecting a genuine departure from isotropy. Indeed these departures are larger than the simulation errors which are approximately 2–3 % as estimated by computing G using (1.8) and (A 5) (see the Appendix). Nonetheless, there is an evident compensation effect which produces an almost perfect equality between $\overline{\epsilon}$ and $\overline{\epsilon_{iso}}$, thus vindicating Antonia *et al.*'s (1998) contention.

Remarkably, compensation comes into play at an early stage of the decay, as can be inferred from figure 1. Note that the $\overline{\omega_i^2}$ data of Antonia *et al.* (1998) also satisfied homogeneity (see figure 6 of Antonia, Orlandi & Zhou 2002) reasonably well in the range $20 \leqslant x/M \leqslant 80$, although the agreement improved towards the end of the range, probably because the spatial resolution of the probe improved with increasing x. It is interesting to note the establishment of a power-law decay with an exponent $n_\epsilon \simeq -2.55$ in the region $x/D \geqslant 30$ which corresponds to a power-law exponent $n \simeq -1.55$ for $\overline{q^2}$. Note that because only a qualitative estimate of n_ϵ is sufficient for the present purpose, the virtual origin x_0 was assumed to be 0. Also, it is clear that a longer distance is required to allow for a full establishment of the power law (as will be seen later).

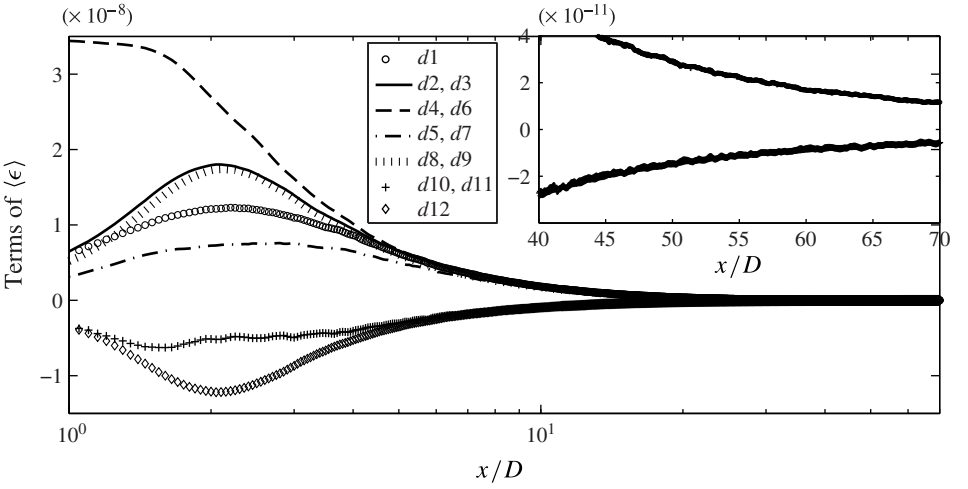

FIGURE 2. Streamwise distribution of all terms of $\overline{\epsilon}$ downstream of the grid. The inset focuses on $40 \leqslant x/D \leqslant 70$; the terms are ordered as in (3.1).

A comment needs to be made with regard to (3.1) and the determination of $\overline{\epsilon}$ from the three-component vorticity probe of Antonia *et al.* (1998). These authors showed that, by assuming incompressibility, terms $d2$ and $d3$ can be obtained via the following relation:

$$2\overline{u_{2,2}^2} + 2\overline{u_{3,3}^2} = 2\overline{u_{1,1}^2} - 4\overline{u_{2,2}u_{3,3}}. \tag{3.2}$$

Assuming homogeneity in the transverse (y, z)-plane, the equality

$$\overline{u_{2,2}u_{3,3}} = \overline{u_{2,3}u_{3,2}} \tag{3.3}$$

should hold. After substituting (3.3) into (3.2), one can obtain

$$\begin{aligned}\overline{\epsilon}_{hom,yz} \;=\; \nu(&4\overline{u_{1,1}^2} + \overline{u_{1,2}^2} + \overline{u_{2,1}^2} + \overline{u_{1,3}^2} + \overline{u_{3,1}^2} + \overline{u_{2,3}^2} + \overline{u_{3,2}^2} \\ &+ 2\overline{u_{1,2}u_{2,1}} + 2\overline{u_{1,3}u_{3,1}} - 2\overline{u_{2,3}u_{3,2}}),\end{aligned} \tag{3.4}$$

the subscript hom, yz standing for homogeneity in the (y, z)-plane. In the present grid turbulence, where the y- and z-directions are 'equivalent', one can expect expression (3.3) to be true in planes perpendicular to the main flow. This is indeed observed in figure 3 which shows that the ratio $\overline{u_{2,2}u_{3,3}}/\overline{u_{2,3}u_{3,2}}$ is almost equal to 1 immediately downstream of the grid and remains equal to 1 for $x/D \geqslant 10$. This result explains the good agreement between $\overline{\epsilon}$ and $\overline{\epsilon}_{hom}$ observed in figure 1, even though lateral homogeneity is not quite satisfied in the region $0 \leqslant x/D \leqslant 1$. It further implies that lateral homogeneity at small scales can be well-approximated even though the flow exhibits large-scale anisotropy. This has relevant implications for the measurement of $\overline{\epsilon}$ in turbulent wall flows such as a channel and a boundary layer. Away from the wall and while the large-scale anisotropy is still important, one can estimate $\overline{\epsilon}$ using expression (3.4) if the homogeneity is valid at small scales; this of course requires that all terms of (3.4) be measured. Antonia *et al.* (1998) demonstrated that this is

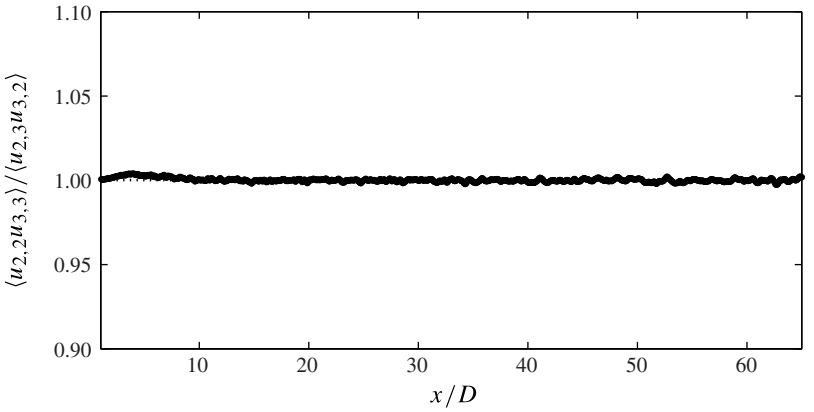

FIGURE 3. Ratio $\overline{u_{2,2}u_{3,3}}/\overline{u_{2,3}u_{3,2}}$.

possible with the used of eight hot wires (four X-probes). They also measured $\overline{\epsilon}$ using the turbulent kinetic energy transport equation ((9.1) in their paper) and found $\overline{\epsilon}_{hom,yz} \simeq \overline{\epsilon}$. Unpublished DNS data in a turbulent channel flow by Abe (Private communication) indicate that (3.3) is closely satisfied for $y/h \geqslant 0.1$ (y is the distance to the wall and h is the half-width of the channel).

4. The transport equation for $\overline{\epsilon}$

The peak in $\overline{\epsilon}$ at $x/D \simeq 2$ indicates that the production (term T_2 in (1.5)) is likely to dominate the transport equation of $\overline{\epsilon}$ in the early stage of decay. This is indeed observed in figure 4 where all the terms on the right-hand side of (1.5), except T_{1a}, T_{1b} and T_{1c}, are reported. The sum $T_1 = T_{1a} + T_{1b} + T_{1c}$ (not reported here), obtained by summing the remaining terms of (1.5) quickly becomes negligible, as can be inferred from figure 5, which shows $-U_0(\partial\overline{\epsilon}/\partial x)$, $-(T_2 + T_3 + T_4 + T_5 + T_6)$ and $-T_6$ (which is only shown for comparison). The good balance between the left- and right-hand sides of (1.5) is a measure of the accuracy of the simulation.

In the region $0 \leqslant x/D \leqslant 30$, all the terms of the transport equation (1.5) contribute to the budget, except the viscous diffusion (T_5) which is practically zero everywhere. While the turbulent diffusion (T_3) is positive up to $x/D \approx 1.6$ before becoming and remaining negative throughout the decay, the pressure term (T_4) has an opposite behaviour. It is clear that the terms T_2 and T_6 dominate the budget; they are dominant throughout the decay (figure 4), suggesting that the stretching of vorticity, i.e. the production of intense 'spotty' vorticity (BT47), and the destruction of vorticity, through viscosity, control the turbulence decay. In particular, these two mechanisms are very important in the region $x/D \leqslant 5$ (figure 4), with the production being stronger, leading to an intensification of the turbulence. Not surprisingly, the location $x/D \simeq 2$, where T_2 is largest, is the same as that where $\overline{\epsilon}$ is maximum. However, for larger x/D, the term T_6 becomes larger than T_2, reflecting the dominance of the destruction by viscosity over production, thus constraining the turbulence to decay. Although it decreases, T_2, which represents both the stretching (positive) and compression (negative) of vorticity, remains positive, implying that stretching occurs more frequently than compression.

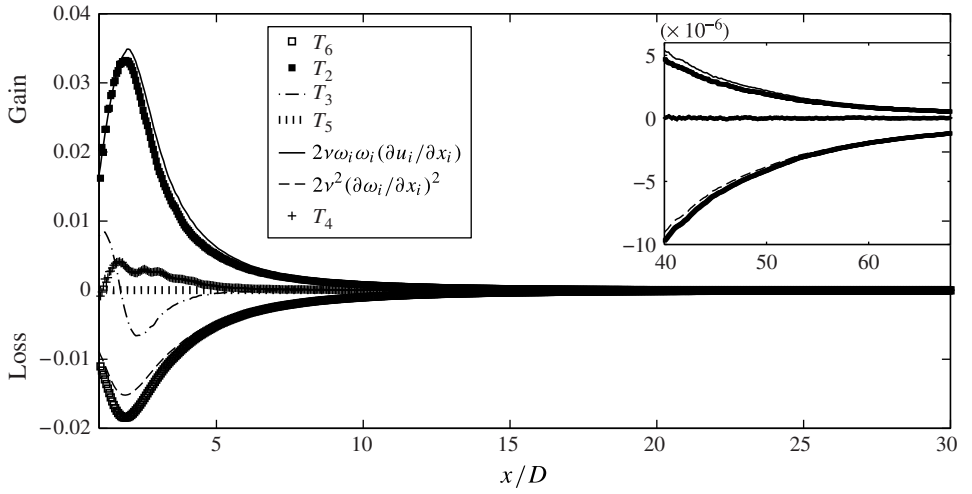

FIGURE 4. Terms in the transport equations of $\overline{\epsilon}$ ((1.2) and (1.5)):T_2 = production of dissipation by turbulent stretching; T_3 = diffusion of dissipation by turbulence; T_4 = dissipation/pressure gradient correlation; T_5 = viscous diffusion; T_6 = destruction of dissipation. Inset: range $40 \leqslant x/D \leqslant 70$. The data are normalized by (U_0^4/D^2).

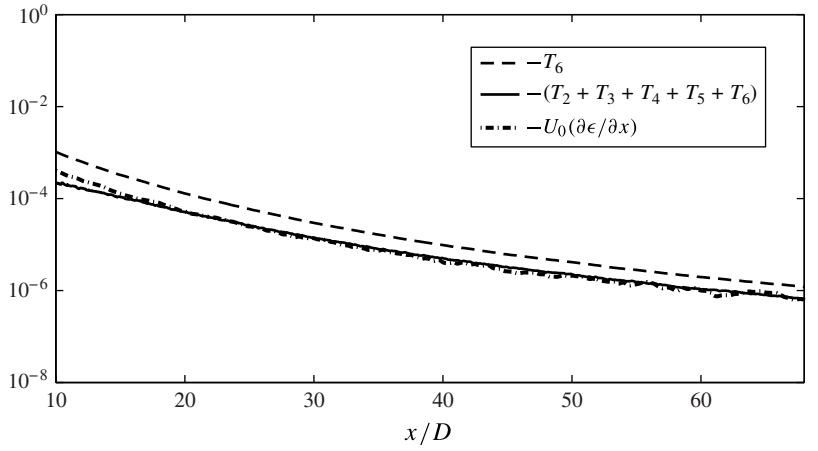

FIGURE 5. Comparison between $U_0(\partial\overline{\epsilon}/\partial t)$, $(T_2+T_3+T_4+T_5+T_6)$ and T_6. The data are normalized by (U_0^4/D^2).

Recalling that all terms of (1.5) are averaged in a plane perpendicular to the mean flow, the streamwise evolution of the term T_3 in figure 4 suggests

$$\int_0^\infty T_3 \mathrm{d}x = \int_\Omega T_3 \mathrm{d}\Omega = 0, \tag{4.1}$$

where Ω is the volume $70D \times 12D \times 12D$, i.e. the computational domain behind the grid. This relation implies that the overall contribution of the turbulent diffusion of $\overline{\epsilon}$

within the entire turbulent field is zero. This is consistent with the following analysis. In the present turbulent flow, the term T_3 takes the form

$$-\frac{\partial\overline{\epsilon u_k}}{\partial x_k}=-\frac{\partial\overline{\epsilon u}}{\partial x}. \tag{4.2}$$

Indeed, averaging over a plane perpendicular to the mean flow erases any lateral inhomogeneity and leads to $-\partial\overline{\epsilon v}/\partial y=-\partial\overline{\epsilon w}/\partial z=0$. Integrating (4.2) with respect to x leads to $[\overline{\epsilon u}]_0^\infty=0$ if $\overline{\epsilon u}=0$ at $x=0$ and $x=\infty$, which one expects to be the case. It is less obvious whether integration of the T_4 term with respect to x yields zero or not. In the present flow, T_4 takes the form:

$$T_4=-\frac{4\nu}{\rho}\frac{\partial}{\partial x}\overline{\left(\frac{\partial u}{\partial x_j}\frac{\partial p}{\partial x_j}\right)}, \tag{4.3}$$

where the continuity equation, $u_{i,j}=0$, has been used in conjunction with the permutation $\partial\overline{A}/\partial x_i=\overline{\partial A/\partial x_i}$. After integration of (4.3), one obtains

$$\int_0^\infty T_4\mathrm{d}x=\left[\frac{4\nu}{\rho}\overline{\left(\frac{\partial u}{\partial x_j}\frac{\partial p}{\partial x_j}\right)}\right]_0^\infty. \tag{4.4}$$

While $[(4\nu)/\rho\overline{(\partial u/\partial x_j)(\partial p/\partial x_j)}]=0$ for $x=\infty$ is supported by the asymptotic behaviour of T_4 at large x/D, it is not evident whether $[(4\nu)/\rho\overline{(\partial u/\partial x_j)(\partial p/\partial x_j)}]=0$ or not when $x/D=0$. Nevertheless, the overall contribution of T_4 is without doubt small. Note that the contribution of both T_3 and T_4 is localized in a relatively short region ($0\leqslant x/D\leqslant 7$) downstream of the grid, where any gain or loss of $\overline{\epsilon}$ by the turbulent diffusion is offset, at least in part, by the pressure diffusion. These two terms arise in this region because the turbulence is strongly non-homogeneous. Still, their net contribution to the transport of $\overline{\epsilon}$ as the turbulence evolves from its birth to its death is relatively weak, if not negligible. This shows that even at a low Reynolds number, the transport equation of $\overline{\epsilon}$ can be remarkably well-represented by a much simplified form of (1.5) where only the terms T_2 and T_6 are retained on the right-hand side of the equation.

5. Simplified form of the transport equation of $\overline{\epsilon}$

The previous section showed that (1.5) can be simplified to

$$\overline{U_k}\frac{\partial\overline{\epsilon}}{\partial x_k}=\underbrace{-\nu\overline{\left(\frac{\partial u_i}{\partial x_j}+\frac{\partial u_j}{\partial x_i}\right)\left(\frac{\partial u_i}{\partial x_k}\frac{\partial u_k}{\partial x_j}+\frac{\partial u_j}{\partial x_k}\frac{\partial u_k}{\partial x_i}\right)}}_{T_2}\underbrace{-\nu^2\overline{\left[\frac{\partial}{\partial x_k}\left(\frac{\partial u_i}{\partial x_j}+\frac{\partial u_j}{\partial x_i}\right)\right]^2}}_{T_6} \tag{5.1}$$

(the term $\partial\overline{\epsilon}/\partial t$ is zero). While $T_2\approx 2\nu\overline{(\omega_i\omega_j\partial u_i/\partial x_j)}$ and $T_6\approx 2\nu^2\overline{(\partial\omega_i/\partial x_j)\,(\partial\omega_i/\partial x_j)}$, there are some differences close to the grid, which seem to weaken but not vanish as x/D increases, as observed in figure 4. This persistence has yet to be explained. Equation (5.1) shows that the production and destruction terms control the decay of $\overline{\epsilon}$

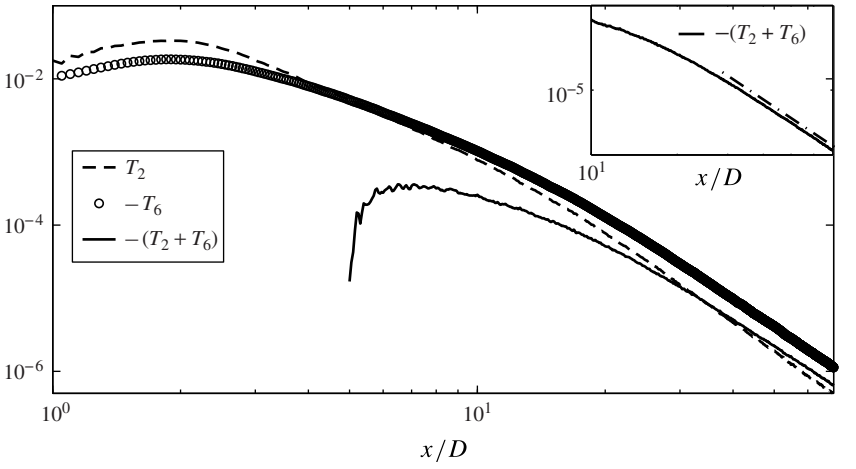

FIGURE 6. Destruction (solid line) and production (dashed line) of $\overline{\epsilon}$ and their sum (circles). The data are normalized by (U_0^4/D^2).

(figure 1), at least in the region $x/D \geqslant 10$. One may then infer that the occurrence of the power-law decay visible in $\overline{\epsilon}$ should be reflected in these terms and their sum. This is indeed observed in figure 6, which shows T_2, $-T_6$ and $-(T_2+T_6)$; all three exhibit a power-law decay. Since $-T_6$ is larger than T_2, it imposes its form of decay on the sum and ultimately on $\overline{\epsilon}$. Note that the sum is negative in the region $1 \leqslant x/D \leqslant 4$, where production is larger than destruction. Of particular interest is that the balance between production and destruction (i.e. $T_2 + T_6$) is not constant during the decay, which seems to be at variance with BT47, who argued that the balance is essentially the same at all stages of the decay. This is important as it signifies that there is no dynamical similarity of those aspects of the turbulence which control the dissipation balance, at least at finite Reynolds numbers.

To gain some insight into the destruction term, T_6, which is critical to the decay of turbulence, the contributions of its individual terms are analysed next. For grid turbulence, where homogeneity is satisfied in planes perpendicular to the main flow and the y- and z-directions are equivalent, T_6 takes the form

$$T_6 = -\nu^2(4\overline{u_{1,11}^2} + 4\overline{u_{2,11}^2} + 8\overline{u_{1,22}^2} + 12\overline{u_{1,12}^2} + 24\overline{u_{2,22}^2} + 24\overline{u_{2,12}^2} + 8\overline{u_{1,12}u_{2,11}} + 16\overline{u_{1,22}u_{2,21}}), \tag{5.2}$$

where the notation $u_{i,kl}$ is used to represent the second-order derivative of the velocity component u_i with respect to the coordinates x_k and x_l. The streamwise variation of each term of (5.2) is displayed on figure 7. Of the eight terms, $24\overline{u_{2,22}^2}$ and $8\overline{u_{1,22}^2}$ are the dominant ones, in particular in the region $20 \leqslant x/D$, which controls the decay of T_6. Notice that all terms appear to follow a power-law decay for $x/D \geqslant 20$. Also evident is the compensation among terms, e.g. $-16\overline{u_{1,22}u_{2,21}}$ balances exactly $12\overline{u_{1,12}^2}$, while $-8\overline{u_{1,12}u_{2,11}}$ balances $4\overline{u_{1,11}^2}$ when $x/D \geqslant 20$. This is reminiscent of the compensation observed among the terms of $\overline{\epsilon}$. It is then reasonable to enquire if T_6 satisfies isotropy. Using the sixth-order isotropic tensor form for $\overline{u_{i,km}u_{j,ln}}$ (first derived by Wyngaard (see Champagne 1978 and Wyngaard 2010), the following isotropic

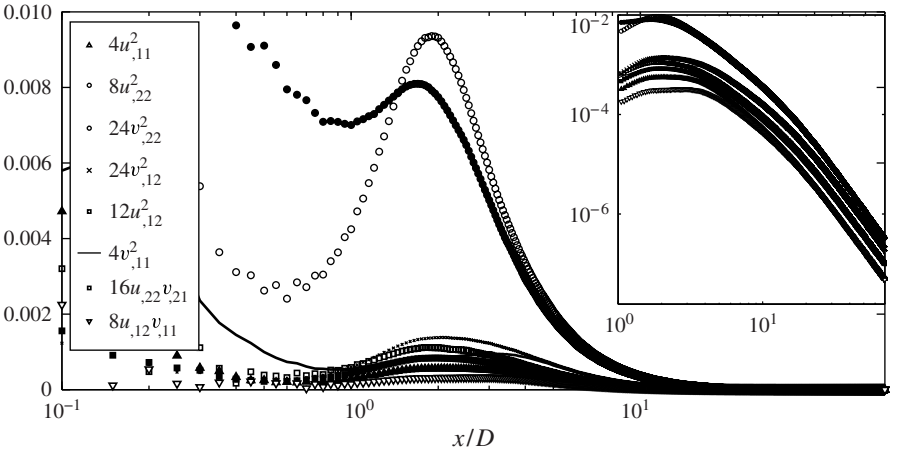

FIGURE 7. Streamwise variation of all terms in (5.2).

relations among the second-order velocity derivatives are obtained:

$$\left.\begin{aligned}
\overline{u^2_{1,22}} &= 3\overline{u^2_{1,11}},\\
\overline{u^2_{1,12}} &= 2\overline{u^2_{1,11}}/3,\\
\overline{u^2_{2,22}} &= \overline{u^2_{1,11}},\\
\overline{u^2_{2,11}} &= 3\overline{u^2_{1,11}},\\
\overline{u^2_{2,12}} &= 2\overline{u^2_{1,11}}/3,\\
\overline{u_{1,12}u_{2,11}} &= -\overline{u^2_{1,11}}/2,\\
\overline{u_{1,22}u_{2,21}} &= -\overline{u^2_{1,11}}/2,
\end{aligned}\right\} \tag{5.3}$$

and are reported in figure 8. Isotropy is not as well-satisfied for $\overline{u^2_{2,22}}/\overline{u^2_{1,11}}$ and $(1/3)\overline{u^2_{1,22}}/\overline{u^2_{1,11}}$ as for the other ratios. For example, over the region $x/D \geqslant 50$, isotropy is satisfied by $\overline{u^2_{2,22}}/\overline{u^2_{1,11}}$ to within 13 %, and by $-2\overline{u_{1,12}u_{2,11}}/\overline{u^2_{1,11}}$ to within 5 %. There is a general tendency for isotropy to improve as x/D increases. If isotropy applies, (5.2) simplifies to

$$T_{6,iso} = -84\nu^2\overline{u^2_{1,11}}. \tag{5.4}$$

This is compared to T_6 in figure 9. Not surprisingly, the departure from isotropy exhibited by the individual terms of T_6 (figure 8) is also observed in $T_{6,iso}$, which does not follow T_6 exactly. Nevertheless, the difference weakens with increasing x/D; at $x/D = 10$ and 65, $T_{6,iso}$ is approximately 20 % and 9 % larger than T_6, respectively, mirroring the improvement in isotropy of the individual terms of T_6 as x/D increases. The present results corroborate the grid turbulence results of Antonia *et al.* (1998) who measured $\overline{\omega^2_{2,1}}$, $\overline{\omega^2_{3,1}}$, $2\overline{\omega^2_{1,1}}$, three of the destruction components as expressed by the second term on the right of (1.2). They showed that the isotropic relation

$$\overline{\omega^2_{2,1}} = \overline{\omega^2_{3,1}} = 2\overline{\omega^2_{1,1}} \tag{5.5}$$

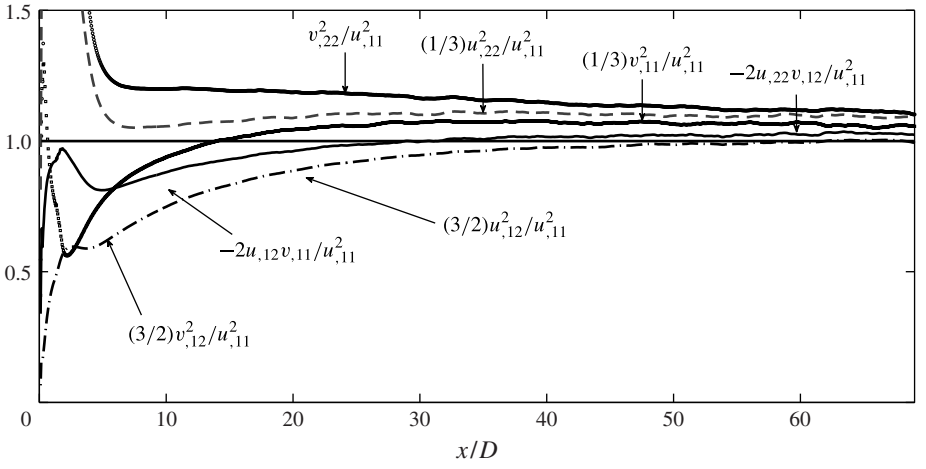

FIGURE 8. Streamwise variation of the ratios $\overline{u_{i,km}u_{j,ln}}/\overline{u^2_{1,11}}$ given in (5.3).

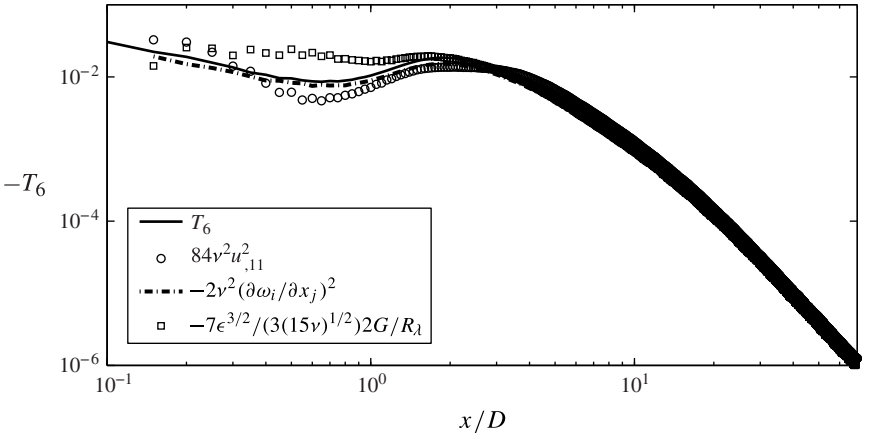

FIGURE 9. Comparison between the actual destruction term ($-T_6$) and its isotropic expression ($84\overline{u^2_{1,11}}$). Also shown are other forms of the destruction term given by the second term on the right-hand side of (1.2) and $2f_\epsilon G/R_\lambda$ from (1.7)). The data are normalized by (U_0^4/D^2).

was verified to within $\pm 10\,\%$. Also reported in figure 9 are the other forms of the destruction term given by the second term on the right-hand side of (1.2) and $2f_\epsilon G/R_\lambda$ (f_ϵ is the factor in front of the parentheses in (1.7)). Altogether, T_6, $2f_\epsilon G/R_\lambda$, and $2\nu^2\overline{\left(\partial\omega_i/\partial x_j\right)\left(\partial\omega_i/\partial x_j\right)}$ are relatively close to each other for $x/D \geqslant 4$, although T_6 remains slightly larger than the other two for $x/D \geqslant 15$. Interestingly, the difference between T_6 and $2f_\epsilon G/R_\lambda$ reflects the anisotropy of the large scales as expressed by the difference between the Reynolds normal stresses $\overline{u^2}$ and $\overline{v^2}$. This difference remains constant downstream of the grid; its magnitude $R = \overline{v^2}/\overline{u^2} = 0.87$ is typical of grid turbulence measurements (Lavoie, Djenidi & Antonia 2007). This can be seen as follows: isotropy at large scales implies $\overline{q^2_{iso}} = 3\overline{u^2}$. However, for grid turbulence, $\overline{u^2} > \overline{v^2}(\overline{v^2} = \overline{w^2})$ which leads to $\overline{q^2} = \overline{u^2}(1 + 2R)$. For the present

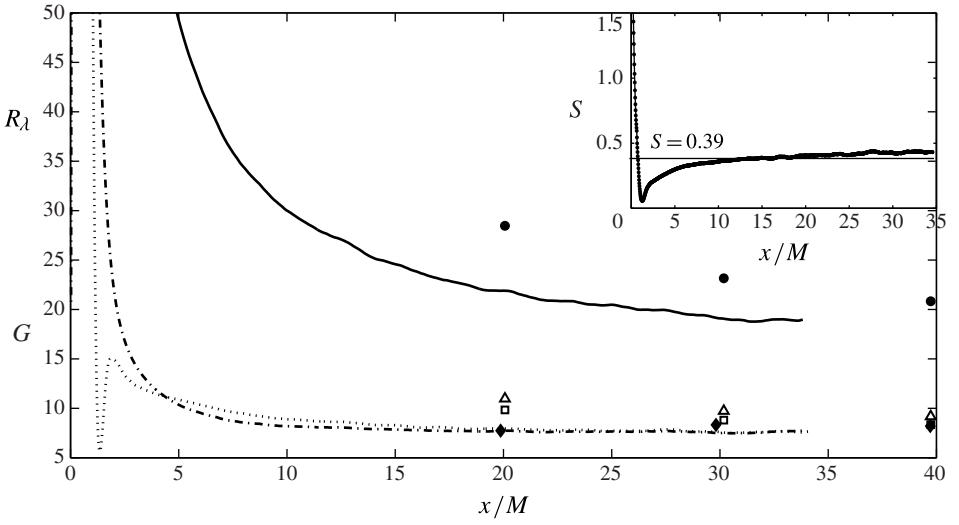

FIGURE 10. Variation of R_λ and G with x/M. Note that we used x/M rather than x/D for a better comparison with the measurements. R_λ: LBM (solid line), BT47 (●); G computed with (1.8): LBM (dashed line), BT47 (♦). G computed with (1.10): dotted-dashed line, LBM; △, BT47 with $S = 0.49$; □, BT47 with $S = 0.39$. Inset: variation of S (LBM) with x/M; the line $S = 0.39$ is used only for reference.

simulation, $\overline{q^2} = 2.74\overline{u^2}$, which is 8.6 % lower than $\overline{q^2_{iso}}$. The low level of anisotropy of the small scales appears to be constant with the downstream distance, merely echoing the constancy of global anisotropy. One expects the small scales to become increasingly less affected by the large scales as the Reynolds number increases, with a subsequent continuous improvement in isotropy. Collectively, the results reported in figures 4 and 9 underline the correspondence between the individual terms of (1.2) and (5.1) despite the low value of the Reynolds number. In other words, the present data justify the use of (1.2) as a reliable surrogate for (1.5) in low-Reynolds-number grid turbulence. This has implications for grid turbulence measurements where R_λ is often not much greater than 50, and which are limited to only a few quantities.

6. Relationship to the power-law decay

For high-Reynolds-number homogeneous and isotropic turbulence, (5.1) becomes exactly (1.7), which is equivalent to (1.10) if turbulence decays according to a power law (i.e. $\overline{q^2} \sim x^n$ or $\overline{\epsilon} \sim x^{n-1}$ with $n < 0$), and $\overline{\epsilon} = \nu\overline{\omega_i\omega_i}$. Thus the equation can be used for estimating G, once R_λ and S are known. This, however, requires knowledge of n, which must be determined independently. BT47 used such a procedure with $n = -1$. Figure 10 compares the values of G calculated with (1.8) and (1.10) for both BT47 ($R_M = 5620$) and the LBM simulation; R_λ is also reported in the figure. Arguing that S is an absolute constant, independent of R_M, BT47 used $S = 0.39$, even though their measurements for $R_M = 5620$ indicated a value of approximately 0.49 for S. The value 0.39 is the average of S measured over the range $R_M = 4.4 \times 10^3$ to 4.4×10^4. We also calculated G with the data of BT47 but using $n = -1$ and $S = 0.49$ and report the results in figure 10. For the LBM data we used $n = -1.55$ and the actual values of S (shown in the inset in figure 10). Although the numerical data cover a shorter

downstream distance than the experimental data, a comparison between the two sets of data is instructive. The difference in the magnitude of R_λ between measurement and simulation reflects different initial conditions (e.g. R_M and grid geometry). While not shown in the figure, the measurements of BT47 show that both R_λ and G are approximately constant for $x/M \geqslant 40$. BT47 used analogue differentiators to measure S and G and indicated that their differentiating circuit is susceptible to amplifier noise that can increase the uncertainty in their estimates of G especially when the turbulence intensity is low. Since BT47 did not provide spectra, it is not possible to check their values of G via the relation

$$G = \frac{\displaystyle\int_0^\infty E_u(k_1)\mathrm{d}k_1 \int_0^\infty k_1^4 E_u(k_1)\mathrm{d}k_1}{\left[\displaystyle\int_0^\infty k_1^2 E_u(k_1)\mathrm{d}k_1\right]^2} \tag{6.1}$$

(see the Appendix). More recent experimental data (Zhou *et al.* 2000; Zhou, Antonia & Chua 2002; Lee *et al.* 2014) show that R_λ actually decreases with increasing x/M, albeit slowly, while G is almost constant. Unfortunately, the short x/M range of the numerical data prevents drawing a definitive conclusion on this issue. Nonetheless, the conclusion that can be drawn is that for $x/M \geqslant 20$, it is impossible to distinguish between the directly estimated value of G and that calculated with (1.10). This is a very important result because while (1.7) and (1.10) were used for analysing both experimental (e.g. BT47, Antonia *et al.* 2004, Lee *et al.* 2014) and numerical (Antonia & Orlandi 2004; Mansour & Wray 1994) data, they have not been verified previously. The present results clearly confirm that (1.7) and (1.10) are appropriate for investigating decaying turbulence downstream of a grid or in a three-dimensional periodic box.

The measured R_λ of Zhou *et al.* (2002) shows a decrease, albeit at a smaller rate than observed by Zhou *et al.* (2000). Antonia *et al.* (2004) argued that, according to (1.10), G varies linearly with R_λ or the product SR_λ if S is not constant. Regarding the BT47 data, it is quite remarkable that G calculated with (1.10) and $S = 0.49$ is approximately 15 % larger than the directly estimated G, while the calculated G with $S = 0.39$ is only approximately 3 % higher. Unfortunately, we can only speculate as to the reasons why the agreement is better with $S = 0.39$ instead of the actual value $S = 0.49$. Aside from the likely systematic experimental errors, one can point to the use of $n = -1$. It is now well-accepted that a value of -1 for n corresponds to complete self-preservation and is unlikely to be found at finite Reynolds numbers; so far $n = -1$ has not been obtained experimentally or by DNS. Using a fixed-point analysis, Speziale & Bernard (1992) showed that a power-law decay $\overline{q^2} \sim t^{-1}$ is consistent with completely self-preserving decay at very high Reynolds numbers, as was inferred earlier by Dryden (1943) from a self-preserving analysis of the Kármán–Howarth equation. In this case, R_λ must remain constant. The good match between the numerical values of G calculated with (1.8) and (1.10) implies that -1.55 is a reasonably close estimate of n, which can be also calculated as follows:

$$n = \frac{1}{1 + \frac{7}{30}(SR_\lambda - 2G)}. \tag{6.2}$$

The variation of $-n$ with x/M inferred from (6.2) and the numerical data for S, R_λ and G is reported in figure 11. For $x/M > 25$, $-n$ is only approximately 6.5 % higher

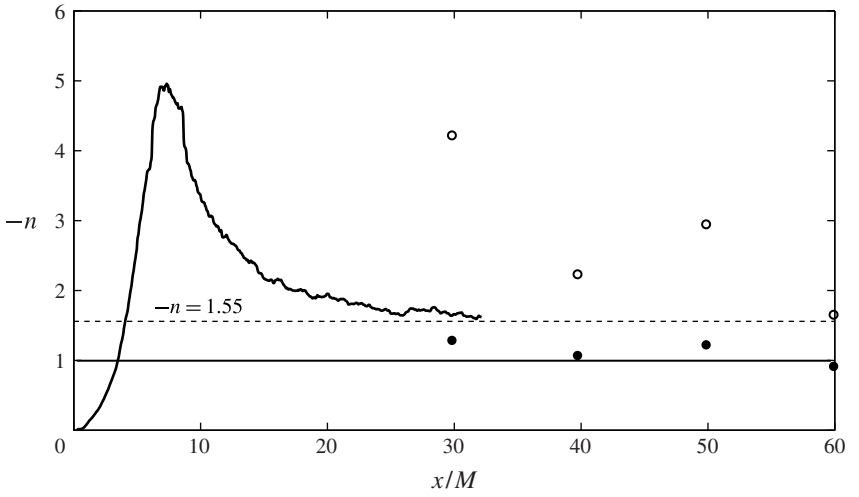

FIGURE 11. Variation of $-n$, computed from (6.2), with x/M. Solid line: LBM. Symbols: BT47 for $R_M = 5620$, and ○, $S = 0.49$; ●, $S = 0.39$.

than 1.55, reinforcing not only the internal consistency of the data but also that (6.2) provides a reliable means for estimating n without the need of knowing x_0, the virtual origin. The value of $-n \simeq 1.6$ is larger than that commonly measured (1.1–1.4) in wind tunnel experiments (Mohamed & LaRue 1990; Lavoie *et al.* 2007) and reflects the low value of R_λ. Figure 11 also reports n calculated with (6.2) for the data of BT47 for $R_\lambda = 5620$ with $S = 0.39$ and 0.49. While $S = 0.39$ leads to $n = -1.16$, $S = 0.49$ yields rather large values of n. This inconsistency reveals the difficulty in measuring adequately both G and S and the need to run consistency checks to ensure reliable results; (1.10) or (6.2) could be used for such consistency checks.

Returning to (5.1), one can observe that the decay of $\overline{\epsilon}$, and ultimately that of $\overline{q^2}$, is controlled by the imbalance between production and destruction, T_2 and T_6, respectively (or S and G in the case of (1.7)). An interesting consequence is that if the decay follows a power law, then the exponent n must be affected by that imbalance as seen in (6.2). The effect of initial conditions is felt through S and G. According to (1.7), $S - 2G/R_\lambda = \text{const.}$ implies a power-law exponent of -1. However, when $S - 2G/R_\lambda$ is not constant, the equation may still lead to a power-law decay if $S - 2G/R_\lambda$ varies like x^γ. This is supported by the present LBM data reported in figure 12, which shows the variation of $-(S - 2G/R_\lambda)$ with x/D in log–log scale. There is a clear linear region when $x/D > 30$, which corresponds also to the region where a power-law decay is observed in $\overline{\epsilon}$ (see figure 1). The slope (i.e. γ) of the linear region is approximately 0.33. Integration of (1.7) with respect to x after substituting $S - 2G/R_\lambda \sim x^\gamma$ into the equation, yields $\overline{\epsilon} \sim x^{-2(\gamma+1)}$ (Lee *et al.* 2014). Since $\overline{\epsilon} \sim x^{n-1}$, it follows that $\gamma = -(n+1)/2$; for $\gamma = 0.33$, $n = -1.66$. Not surprisingly, this value is about the same as that calculated with (6.2) (see figure 11), providing further confidence in the validity of (1.7) at low Reynolds numbers, and that (1.10) (or (6.2)) is an exact expression in which n, S and G are intimately related. Interestingly, this result would entail that the small-scale motion may play, along with the large-scale motion, a role in establishing the value of n, a result at odds with the more traditional thinking that n is solely controlled by the large-scale structures. Mansour & Wray (1994) argued that the difference between the production and destruction rates of $\overline{\epsilon}$, namely $C_{\epsilon 2}$, not

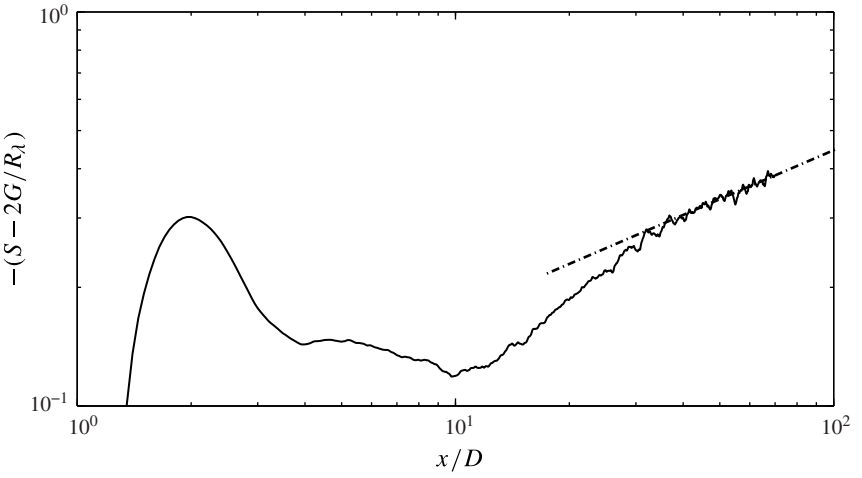

FIGURE 12. $-(S-2G/R_\lambda)$ as a function of x/M. The straight line is used as a visual aid only.

only is sensitive to the initial conditions, but also depends on both the large scales (through $\overline{q^2}$ in (1.4)) and the small scales. Lee *et al.* (2014) also argue that their grid turbulence measurements support the idea that one cannot overlook the role of the small scales in determining or at least maintaining the decay rate exponent of $\overline{q^2}$.

Although the present work is not concerned with the initial and final periods of decay, it is nevertheless of interest to discuss the transport equation (1.10) with respect to these decay stages. Recasting the equation as

$$\frac{G}{R_\lambda} = \frac{15}{7}\left(\frac{n-1}{n}\right)\frac{1}{R_\lambda} + \frac{S}{2}, \tag{6.3}$$

Lee *et al.* (2014) compiled grid turbulent data (for both passive and active grids) for R_λ ranging from approximately 10 to 1000 and plotted them along with their own measurements in the form of G/R_λ as a function of R_λ. We reproduce a selection of their data sets in figure 13, which includes the data of BT47 ($R_\lambda = 5620$), Zhou *et al.* (2000, 2002) and the present LBM data (only for $x/M \geqslant 15$). The lines, computed with (6.3), are presented to illustrate the effect of n, S and R_λ on the behaviour of the ratio G/R_λ. In computing the lines, values of n and S are assumed to be constant for all R_λ, an assumption which is clearly not valid. This however does not affect a qualitative discussion on the asymptotic states. When R_λ is very large, the solution should approach the result corresponding to stationary turbulence, namely $G/R_\lambda = S_\infty/2$. The present LBM data fall within the range of existing data at similar R_λ (see inset of figure 13). Two important observations can be drawn from the figure: (i) $G/R_\lambda \to \infty$ when $R_\lambda \to 0$ and (ii) $G/R_\lambda \to$ const. when $R_\lambda \to \infty$. The first observation indicates that G approaches a non-zero value in the final period of decay, or at least that R_λ decreases much more rapidly than G. The second shows that $G \to 0.5 S_\infty R_\lambda$ at very large R_λ, i.e. G varies linearly with R_λ. This trend is supported by recent experimental results, e.g. the data gathered by Lee *et al.* (2014) up to $R_\lambda \simeq 10^3$, and the EDQNM results of Meldi & Sagaut (2013). Associated with this trend is the approach of n to its asymptotic value of -1 (e.g. Antonia *et al.* 2013;

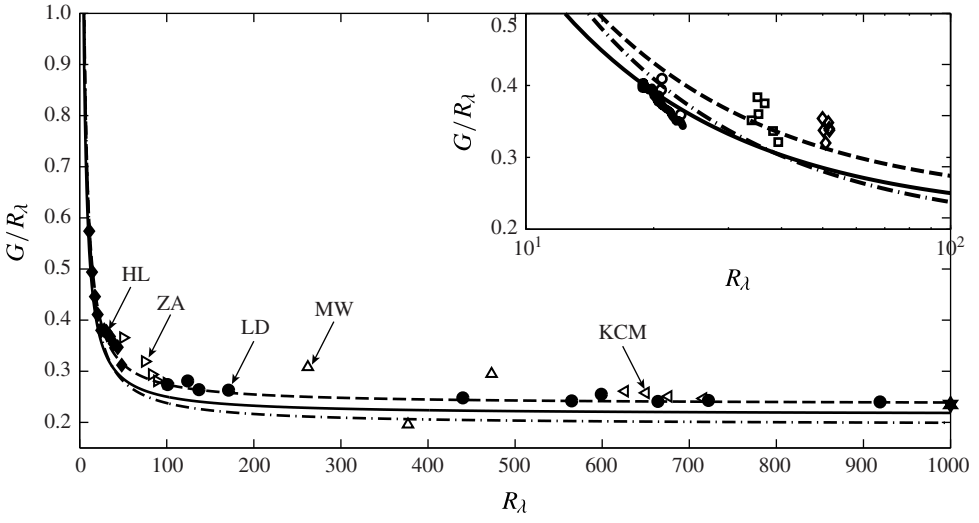

FIGURE 13. G/R_λ as a function of R_λ. The data symbols are extracted from Lee *et al.* (2014). LD: Larssen & Devenport (2011); ZA: Zhou & Antonia (2000); HL: Huang & Leonard (1994); MW: Mydlarsky & Warhaft (1996); KCM: Kang, Chester & Meneveau (2003). Inset: short thick solid line, LBM; ○, BT47; □, Zhou *et al.* (2002); ◇, Zhou *et al.* (2000); to facilitate viewing a log scale is used for the abscissa. The lines are computed with (6.3): solid, $n=-1.55$, $S=0.43$; dot-dashed, $n=-1.0$, $S=0.39$, dashed, $n=-1.2$, $S=0.50$.

Meldi & Sagaut 2013). Further, (6.3) can be reformulated as

$$S-2\frac{G}{R_\lambda}=\frac{30}{7}\left(\frac{n-1}{n}\right)\frac{1}{R_\lambda}, \tag{6.4}$$

which indicates that $S-2G/R_\lambda\to 0$ asymptotically as $R_\lambda\to\infty$, leading to stationary turbulence. Thus, one expects the decay term in the $\overline{\epsilon}$-transport equation (represented by the right-hand side of (6.4)) to decrease with increasing Reynolds number, implying that the small-scale turbulence approaches stationarity (or universality) in accordance with the Kolmogorov theory (Kolmogorov 1941). Note that if the turbulent kinetic energy decays like x^{-1}, the flow is expected to satisfy complete self-similarity and R_λ remains constant with x. This is yet to be observed. It is worthwhile pointing out that (6.4) is an exact equation, and as such imposes an exact dynamical constraint on the asymptotic behaviours of S and G as $R_\lambda\to\infty$.

Equation (1.10) can be further exploited for discussing the decay as R_λ decreases. One may consider two limiting cases: (i) $S=\beta R_\lambda^\alpha$ ($\beta\geqslant 0$ and $\alpha\geqslant 0$) or (ii) $S=$ const. Mansour & Wray (1994) (see also Tavoularis *et al.* 1978) showed that for $R_\lambda\leqslant 5$, S decreases with decreasing R_λ, according to a power law $S\sim R_\lambda^m$, where the positive exponent m is not constant in the range $1\leqslant R_\lambda\leqslant 25$. Since S is related to the spectral transfer of energy (Tavoularis *et al.* 1978), the reported decrease of S as R_λ decreases reflects the gradual weakening of the energy transfer $T(k)$ from large to small scales; ultimately, the energy transfer should become negligible, implying a lack of interaction between vortices. More recently, the EDQNM of Meldi & Sagaut (2013) shows that $S\simeq R_\lambda$ when $R_\lambda<1$. On the other hand, using Heisenberg's spectral theory, Reid (1956) and Lin & Reid (1963) predict a non-zero S_0 as $R_\lambda\to 0$. Regardless of the

actual value of S when $R_\lambda \to 0$, both cases imply that $SR_\lambda \ll 2G$ in the final period of decay, which is consistent with the data in figure 12. Accordingly, (6.2) reduces to

$$n = \frac{1}{1 - \frac{7}{15}G}. \tag{6.5}$$

Since $n \leqslant -1$, then

$$\frac{15}{7} \leqslant G \leqslant \frac{30}{7}. \tag{6.6}$$

This is in agreement with the result of the fixed-point analysis of Speziale & Bernard (1992) (see also Ristorcelli & Livescu 2004). Expression (6.6) thus reveals that $15/7 \leqslant G_{R_\lambda \to 0} \leqslant 30/7$ as $R_\lambda \to 0$. It is worth comparing this asymptotic behaviour of G with values obtained for two known final periods of decay. According to Batchelor & Townsend (1948*b*), $n = -5/2$ in the final period of decay so that $G_{R_\lambda \to 0} = 3$ or $21/7$, whereas Saffman (1967) found, also for the final period of decay, $n = -3/2$, thus leading to $G_{R_\lambda \to 0} = 25/7$. According to (6.6) both values of G are possible in the final period. Note though that the condition (6.6) imposed on G allows many possible final periods to exist, each likely to be defined by the initial conditions. The above analysis and the data in figure 13 at small R_λ are consistent with G remaining finite and approaching a non-zero value in the limit $R_\lambda \to 0$. Thus, $S = \beta R_\lambda^\alpha$ leads to

$$\frac{\mathrm{d}n}{\mathrm{d}R_\lambda} = \frac{-\frac{7}{30}\beta(\alpha+1)R_\lambda^\alpha}{\left[1 + \frac{7}{30}(\beta R_\lambda^{\alpha+1} - 2G)\right]^2} \tag{6.7}$$

while $S = \text{const.}$ results in

$$\frac{\mathrm{d}n}{\mathrm{d}R_\lambda} = \frac{-\frac{7}{30}S}{\left[1 + \frac{7}{30}(SR_\lambda - 2G)\right]^2}. \tag{6.8}$$

In the limit $R_\lambda \to 0$, equations (6.7) and (6.8) yield $\mathrm{d}n/\mathrm{d}R_\lambda \to 0$ and $\mathrm{d}n/\mathrm{d}R_\lambda \to ((-7/30S)/([1 - 7/15G]^2))$, respectively. Note that the last solution should lead to a small, if not negligible, value of $\mathrm{d}n/\mathrm{d}R_\lambda$. This can be easily seen if we assume $S = 0.5$ (clearly an overestimated value) and use either $G = 3$ or $25/7$. Thus, the power-law exponent n remains approximately constant in the final period of decay as R_λ decreases. Also, one can show that $\mathrm{d}n/\mathrm{d}R_\lambda = 0$ when $R_\lambda \to \infty$ since $G \sim R_\lambda$. This simple analysis reveals how n behaves during the entire process of turbulence decay. In the early stages of the initial period where the Reynolds number is large, the magnitude of n is approximately constant ($\simeq n_\infty$), and likely to be fixed by the initial conditions. As the Reynolds number decreases (with increasing x/M), n decreases to its final period value, n_0, and remains practically constant. This is in agreement with the EDQNM results of Meldi & Sagaut (2013). To date, all experiments on grid turbulence, which are for $R_\lambda \geqslant 30$, report a power-law exponent n of between approximately -1.1 and -1.4. The value of $n = -1.55$ obtained in the present simulations reflects the low value of the Reynolds number. It should decrease further as R_λ decreases to reach its final period value. The actual final value of n when $R_\lambda \to 0$ is yet to measured.

Finally, it is appropriate to comment on (1.7) in relation to turbulence modelling. The widely used turbulence model in CFD is the so-called k–ϵ model. The model

consists of the transport equations for k (or $\overline{q^2}$) and $\langle\epsilon\rangle$. The reliability of the model hinges on a reliable closure of the $\langle\epsilon\rangle$-equation. For HIT, the equation is

$$\frac{\mathrm{d}\overline{\epsilon}}{\mathrm{d}t} = C_{\epsilon 2}\frac{\overline{\epsilon^2}}{\overline{q^2}} \tag{6.9}$$

where $C_{\epsilon 2}(=R_\lambda S - 2G)$ is assumed to be constant at sufficiently high Reynolds number (e.g. Tennekes & Lumley 1974). However, (1.10) leads to

$$C_{\epsilon 2} = \left(\frac{n-1}{n}\right), \tag{6.10}$$

showing that $C_{\epsilon 2}$ is function of the decay exponent, which in turn, as seen above, depends on the Reynolds number. Thus $C_{\epsilon 2}$ cannot be universal. It is likely that it will vary not only from flow to flow, but also from location to location in a given flow. Calibrating the value of the constant $C_{\epsilon 2}$ against grid turbulence data can only lead to an erroneous model constant for other flows. A more reasonable approach is to use the $\langle\epsilon\rangle$-equation, written in a form similar to (1.7), relevant to the flow (e.g. jets, wakes and wall flows) that is being modelled.

7. Conclusions

DNS based on the LBM have been carried out for the turbulence downstream of a grid consisting of flat square elements. The individual terms of $\overline{\epsilon}$ and its transport equation are analysed in detail. The results support the contention of Antonia *et al.* (1998) that there is sufficient compensation among the components of $\overline{\epsilon}$, which produces a near equality between $\overline{\epsilon}$ and its isotropic value, $15\nu\overline{(\partial u/\partial x)^2}$, in the region $x/D \geqslant 10$. However, this near equality is not as good as that between $\nu\overline{\omega_i\omega_i}$ and $\overline{\epsilon}$ across the entire decay range, which indicates that the homogeneity of the small-scale motion is a good approximation despite the non-homogeneity of the mean quantities in the main flow direction. The results also show that there is sufficient compensation among the individual components of the destruction term in the transport equation of $\overline{\epsilon}$. The isotropic form $(-84\nu^2\overline{(\partial^2 u/\partial x^2)})$ of the destruction term is satisfied to better than 10 %, at $x/M = 30$.

For the first time, the equivalence between the general transport equation for $\overline{\epsilon}$ and its isotropic form in low-Reynolds-number grid turbulence is confirmed. This equivalence is important in the context of (low-Reynolds-number) grid turbulence experiments where only the isotropic form of the $\overline{\epsilon}$-transport equation is amenable to measurements. The result is also important because it vindicates the use of (1.7) and (1.10) for analysing experimental data in low-Reynolds-number decaying grid turbulence. In this regard, it is a remarkable achievement that BT47 were able to verify, albeit approximately, (1.10) using grid turbulence measurements.

All the terms in the transport equation of $\overline{\epsilon}$, except for the viscous diffusion term which is practically zero, are important in the region $x/D \leqslant 5$, although the production, due to vortex stretching, and destruction tend to dominate. This reflects the strong inhomogeneity in this region. Beyond this region, the transport of $\overline{\epsilon}$ is mainly controlled by the imbalance, equal to $\overline{U}(\mathrm{d}\overline{\epsilon}/\mathrm{d}x)$, between production and destruction, the latter being larger than the former. While this is consistent with the existing theory of homogeneous and isotropic turbulence (BT47), there is an important difference. The imbalance between the production and destruction is not

constant during the decay, as argued by BT47. The non-constancy implies that the transport of $\overline{\epsilon}$ during its decay is not dynamically self-similar and that the turbulence cannot decay according to a power law (i.e. $\overline{q^2} \sim x^n$) with an exponent n equal to -1. Nevertheless, the turbulence decays according to a power law because the imbalance (e.g. $S + 2G/R_\lambda$) varies as a power of x; the present value of n is actually close to -1.6, a value in keeping with the relatively low Reynolds number of the simulation. The results highlight the importance of the imbalance in establishing the value of n. They also demonstrate for the first time that (1.10) is very closely satisfied in grid turbulence at a small Reynolds number. *A fortiori*, one would expect that the equation will hold at larger Reynolds numbers.

The transport equation, rewritten in (6.2) as an expression for n, has been discussed in the context of $R_\lambda \to 0$. The discussion provides some insight into the behaviour of n during the entire decay process and a yet to be confirmed theoretical result, namely the destruction coefficient G is constant and its a magnitude must lie between 15/7 and 30/7. These two bounds encompass the predictions for G in the final period of decay, given by Batchelor & Townsend (1948*a*,*b*) and Saffman (1967).

Acknowledgement

The financial support of the Australian Research Council is gratefully acknowledged.

Appendix – Accuracy of the computation

Since the present study deals with the small-scale motion and in particular with first- and second-order velocity derivatives, it is important to establish that the computational resolution is adequate. A few checks of the accuracy of the computation are given below.

In grid turbulence, $\overline{\epsilon}$ can be easily and reliably obtained via the turbulent kinetic energy transport equation which is closely approximated by

$$U\frac{\partial q^2}{\partial x} = -\overline{\epsilon}. \tag{A 1}$$

Values of $\overline{\epsilon}$ obtained through different expressions (e.g. $\overline{\epsilon} = \nu\overline{\omega_i\omega_i}$, $\overline{\epsilon} = 15\nu\overline{(\partial u/\partial x)^2}$ or $\overline{\epsilon} = 15\nu\int_0^\infty k_x^2 E(k_x)\mathrm{d}k_x$) can be compared with the value given by (A 1). Figure 14 shows the distribution of $\overline{\epsilon}$ obtained with (A 1) and that calculated from (1.1). Despite the inevitable scatter associated with computing the derivative of q^2 (no smoothing on q^2 and its derivative has been applied), expressions (A 1) and (1.1) are in close agreement for $x/D > 20$, suggesting that the grid resolution is sufficient for calculating $\overline{\epsilon}$ via expression (1.1).

A more stringent assessment of the computational resolution is provided by the velocity spectrum. Figure 15 shows distributions of $E_v(k_y)$ at $x/D = 8.45$, 28.45 and 68.45. The figure shows $E_v(k_y)$ normalized by the Kolmogorov scales (v_K, η) denoted by *; k_y is the wavenumber along a transverse direction and $E_v(k_y)$ is the spectrum of v, defined such that

$$\overline{v^2} = \int_0^\infty E_v(k_y)\mathrm{d}k_y. \tag{A 2}$$

It should be pointed out that we checked that $E_v(k_y) = E_u(k_x)$ (where k_x is the wavenumber along the longitudinal direction and $E_u(k_x)$ is the spectrum of u computed using the time series signal and Taylor's hypothesis). The LBM spectra are computed

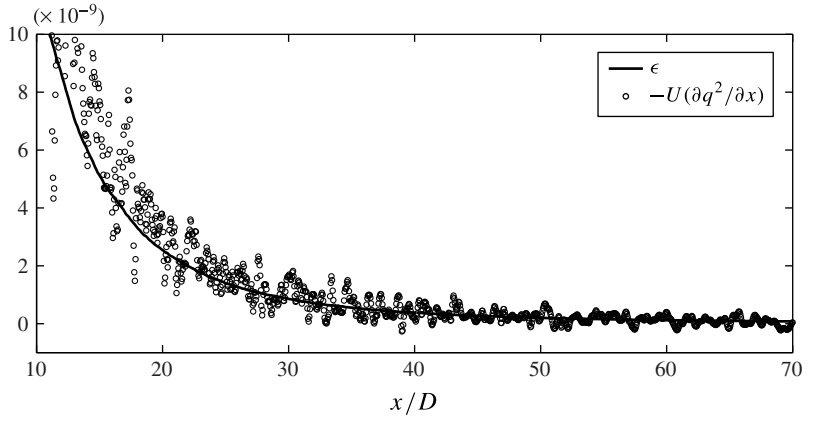

FIGURE 14. Streamwise variations of $\overline{\epsilon}$ and $-U(\partial q^2/\partial x)$.

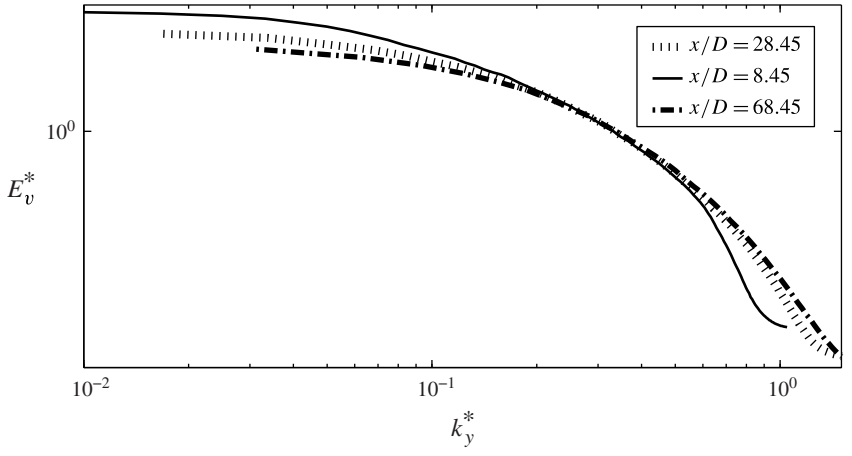

FIGURE 15. Spectra $E_v^*(k_y^*)$ for three x/D values. The symbol * represents the Kolmogorov normalization.

using a fast Fourier transform (FFT) with a Hanning window and an FFT length of 256. The FFT is performed on the transverse velocity along the y-direction using a length $N = 256$. Note that since there are only 240 data points in the transverse direction, the first 16 data points of each segment are added at the other end of the segment. This is consistent with the periodic nature of the boundary conditions used in the simulation. Thus 240 individual spectra are computed for one realization. This is repeated for all realizations recorded (i.e. 40 fields) and averaged to yield the spectra shown in figure 15. At $x/D = 8.45$, the spectrum drops off too quickly at the high wavenumbers reflecting the extra dissipative effect introduced by the LES scheme. This effect is reduced significantly at $x/D = 28.45$ and is not discernible at $x/D = 68.45$. The weakening of the LES dissipative effect on the energy spectra is associated with the improved grid resolution as the distance x/D increases. As stated earlier, the grid resolution, which is also equal to the LES spatial filter (Δ), varies from $\Delta y = 2.9\eta$ at $x/D = 8$ (or $x/M = 4$) to $\Delta y = 0.78\eta$ at $x/D = 68$ (or $x/M = 34$). Such a spatial resolution is common in grid turbulence measurements. For example

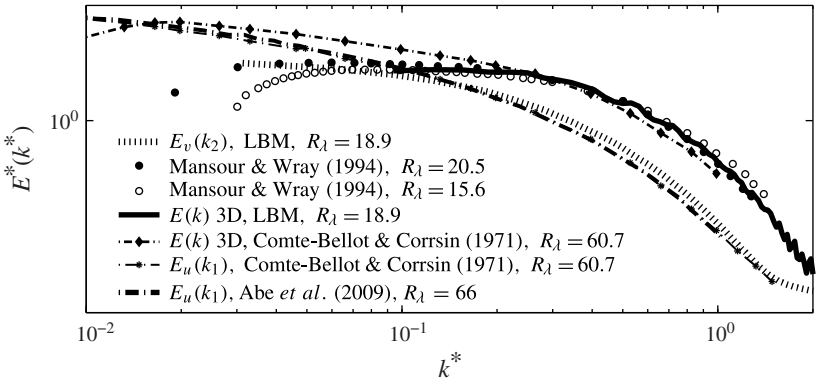

FIGURE 16. Three-dimensional spectra $E^*(k^*)$ and one-dimensional spectra $E_v^*(k_y^*)$. Also shown are data from DNS of Mansour & Wray (1994) in decaying box turbulence and Abe *et al.* (2009) in a turbulent channel flow, and measurements in grid turbulence (Comte-Bellot & Corrsin 1971).

Krogstad & Davidson (2010) reported a ratio l_w/η (l_w is the hot wire length) ranging from approximately 2.6 at their first measurement station ($x/M \approx 35$) to 0.8 at the most downstream portion ($x/M \approx 250$). Similar spatial resolutions (2.1 to 0.86) are reported by Lavoie *et al.* (2007) and (1.4 to 0.5) by Comte-Bellot & Corrsin (1971).

To assess the quality of the computed spectra, the spectrum at $x/D = 68.45$ is compared (figure 16) with that measured by Comte-Bellot & Corrsin (1971) in grid turbulence and that computed (DNS) by Abe, Antonia & Kawamura (2009) in a turbulent channel flow. Also shown in figure 16 are three-dimensional spectra, $E(k)$, for the present LBM, the experiment of Comte-Bellot & Corrsin (1971) in grid turbulence and the DNS (spectral method) of Mansour & Wray (1994) in decaying box turbulence. To compute $E(k)$ we followed Comte-Bellot & Corrsin (1971) and used the isotropic assumption

$$E(k) = \frac{1}{2}k^3 \frac{\partial}{\partial k}\left(\frac{1}{k}\frac{\partial}{\partial k}E_v(k)\right), \tag{A 3}$$

with $k = k_y$.

The difference between the LBM one-dimensional spectrum and that of Comte-Bellot & Corrsin or Abe *et al.* reflects low-Reynolds-number effects, already observed by Mansour and Wray (see also Djenidi, Tardu & Antonia 2013*b*; Kamruzzaman, Djenidi & Antonia 2013). The distributions of $E(k)$ obtained by Mansour & Wray (1994) agree well with the present spectrum at a comparable R_λ.

Clearly, figures 15 and 16 indicate that the LBM resolves the small-scale motions sufficiently accurately, at least for the region $x/D > 8$. The LBM spectra show some attenuation at the higher wavenumbers. This is a combined effect of aliasing and spectral leakage. Aliasing occurs because f_s is smaller than $2f_K$, where $f_s = 1/\Delta y$ and $f_K = 1/\eta$ are the sampling and Kolmogorov frequencies, respectively. Spectral leakage is caused by the discontinuities in the spatial signal of the velocity (figure 17), which result from the non-periodic nature of the individual velocity segments. Note however that spectral leakage is minimized by carrying out the FFT on traces containing only 256 samples and using the Hanning window.

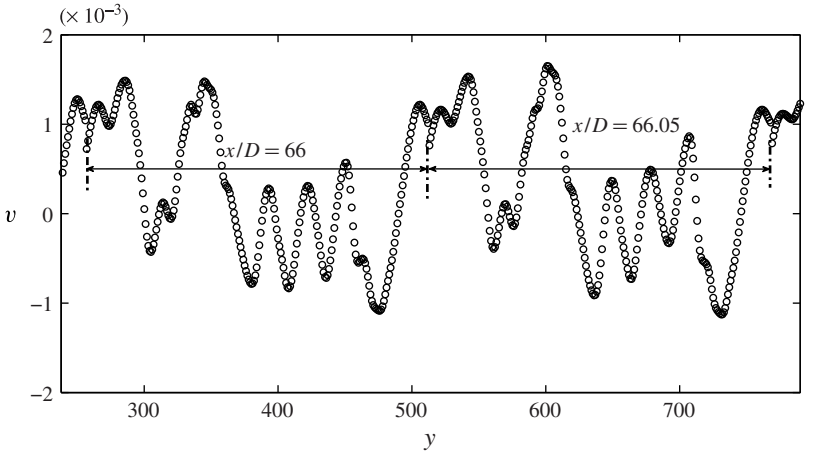

FIGURE 17. Spanwise variation of the transverse velocity v at two consecutive downstream positions, $x/D = 66$ and 66.05.

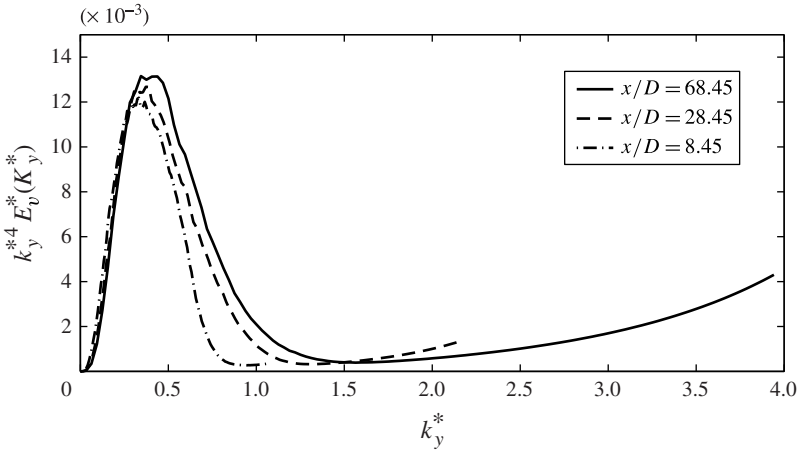

FIGURE 18. k^4-weighed spectra $k_y^{*4} E_v^*(k_y^*)$.

That the small-scale motion is adequately resolved is supported by the data of figure 18 showing distributions of $k_y^4 E_v(k_y)$. In particular, the figure shows that the LBM captures well the zone that contributes most to the integral

$$\int_0^\infty k_y^4 E_v(k_y)\mathrm{d}k_y \tag{A 4}$$

which is used for calculating G

$$G = \overline{u^2}\frac{\displaystyle\int_0^\infty k_y^4 E_v(k_y)\mathrm{d}k_y}{\left[\displaystyle\int_0^\infty k_y^2 E_v(k_y)\mathrm{d}k_y\right]^2}. \tag{A 5}$$

The increase in $k^{*4}E_v^*(k^*)$, where the symbol * represents the Kolmogorov normalization, after it reaches a minimum reflects the aliasing and spectral leakage observed in the spectra and is not physical. There is no 'energy' pile-up even at $x/D = 8.45$ where the relatively poor grid resolution could have been a source of aliasing. Values of G are obtained with (A 5) where the integration is carried out from k_{min} to k_{max} where k_{min} is the lowest wavenumber and k_{max} is the wavenumber where $k_y^{*4}E_v^*(k_y^*)$ reaches its minimum. The values of G thus obtained (11.97, 8.64 and 7.9 at $x/D = 8.45$, 28.45 and 68.45) are slightly (2–3 %) larger than those calculated from (1.8) (11.35, 7.95, 7.53, respectively). This agreement supports the claim that the small-scale motion is adequately resolved.

REFERENCES

ABE, H., ANTONIA, R. A. & KAWAMURA, H. 2009 Correlation between small-scale velocity and scalar fluctuations in a turbulent channel flow. *J. Fluid Mech.* **627**, 1–32.

ANTONIA, R. A., LEE, S. K., DJENIDI, L., LAVOIE, P. & DANAILA, L. 2013 Invariants for slightly heated decaying grid turbulence. *J. Fluid Mech.* **727**, 379–406.

ANTONIA, R. A. & ORLANDI, P. 2004 Similarity of decaying isotropic turbulence with a passive scalar. *J. Fluid Mech.* **505**, 123–151.

ANTONIA, R. A., ORLANDI, P. & ZHOU, T. 2002 Assessment of three-components vorticity probe in decaying turbulence. *Exp. Fluids* **33**, 384–390.

ANTONIA, R. A., SMALLEY, R. F., ZHOU, T., ANSELMET, F. & DANAILA, L. 2004 Similarity solution of temperature structure functions in decaying homogeneous isotropic turbulence. *Phys. Rev.* E **69**, 016305.

ANTONIA, R. A., ZHOU, T., DANAILA, L. & ANSELMET, F. 2002 Scaling of the mean energy dissipation rate equation in grid turbulence. *J. Turbul.* **3**, 1468-5248(02)52345-6.

ANTONIA, R. A., ZHOU, T. & ZHU, Y. 1998 Three-component vorticity measurements in a turbulent grid flow. *J. Fluid Mech.* **374**, 29–57.

BATCHELOR, G. K. & TOWNSEND, A. A. 1947 Decay of vorticity in isotropic turbulence. *Proc. R. Soc. Lond.* A **190**, 534–550.

BATCHELOR, G. K. & TOWNSEND, A. A. 1948*a* Decay of isotropic turbulence in the initial period. *Proc. R. Soc. Lond.* A **193**, 539–558.

BATCHELOR, G. K. & TOWNSEND, A. A. 1948*b* Decay of isotropic turbulence in the final period. *Proc. R. Soc. Lond.* A **194**, 527–543.

BENNETT, J. C. & CORRSIN, S. 1978 Small Reynolds number nearly isotropic turbulence in a straight duct and a contraction. *Phys. Fluids* **21**, 2129–2140.

BRADSHAW, P. & PEROT, J. B. 1993 A note on turbulent energy dissipation in the viscous wall region. *Phys. Fluids* A **5**, 3305–3306.

BURATTINI, P., LAVOIE, P., AGRAWAL, A., DJENIDI, L. & ANTONIA, R. A. 2006 On the power law of decaying homogeneous isotropic turbulence at low R_λ. *Phys. Rev.* E **73**, 066304.

CHAMPAGNE, F. H. 1978 The fine-scale structure of the turbulent velocity field. *J. Fluid Mech.* **86** (1), 67–108.

CHASSAING, P. 2000 *Turbulence en Mecanique des Fluides. (Collection Polytech)*, Cépaduès-Éditions.

CHEN, S. & DOOLEN, G. D. 1998 Lattice Boltzmann method for fluid flows. *Annu. Rev. Fluid Mech.* **30**, 329–364.

COMTE-BELLOT, G. & CORRSIN, S. 1971 Simple Eulerian time correlation of full- and narrow band velocity signals in grid generated, 'isotropic' turbulence. *J. Fluid Mech.* **48**, 273–337.

CORRSIN, S. 1953 Interpretation of viscous terms in the turbulent energy equation. *J. Aeronaut. Sci.* **20**, 853–854.

DJENIDI, L. 2006 Lattice Boltzmann simulation of grid-generated turbulence. *J. Fluid Mech.* **552**, 13–35.

DJENIDI, L. 2008 Study of the structure of a turbulent crossbar near-wake by means of Lattice Boltzmann. *Phys. Rev.* E **77**, 036310.

DJENIDI, L., TARDU, S. & ANTONIA, R. A. 2013*a* Relation between temporal and spatial averages in grid turbulence. *J. Fluid Mech.* **730**, 593–606.

DJENIDI, L., TARDU, S. & ANTONIA, R. A. 2013*b* Breakdown of Kolmogorov's scaling in grid turbulence. In *14th European Turbulence Conference, 10–14 September, Lyon, France* pp. 593–606.

DRYDEN, H. L. 1943 A review of the statistical theory of turbulence. *Q. Appl. Maths* **1**, 7–42.

FRISCH, U., HASSLACHER, B. & POMEAU, Y. 1986 Lattice gas automata for the Navier–Stokes equations. *Phys. Rev. Lett.* **56**, 1505–1508.

AGEORGE, W. K. 1992 The decay of homogeneous isotropic turbulence. *Phys. Fluids* **4**, 1492–1509.

HANJALIC, K. & LAUNDER, B. E. 1972 A Reynolds stress model of turbulence and its application to thin shear flows. *J. Fluid Mech.* **52**, 609–638.

HOU, S., STERLIN, J., CHEN, S. & DOOLEN, G. D. 1996 A lattice Boltzmann subgrid model for high Reynolds number flows. In *Pattern Formation and Lattice Gas Automata* (ed. A. T. Lawniczak & R. Kapral), Field Institute Communications, vol. 6, pp. 151–166. American Mathematical Society, Also arXiv:comp-gas/9401004v1.

HUANG, M.-J. & LEONARD, A. 1994 Power-law decay of homogeneous turbulence at low Reynolds number. *Phys. Fluids* **6**, 3765–3775.

KAMRUZZAMAN, MD., DJENIDI, L. & ANTONIA, R. A. 2013 Behaviours of energy spectrum at low Reynolds numbers in grid turbulence. *International Journal of Mechanical, Industrial Science and Engineering* **7**, 472–476.

KANG, H. S., CHESTER, S. & MENEVEAU, C. 2003 Decaying turbulence in an active-grid generated flow and comparisons with large-eddy simulation. *J. Fluid Mech.* **480**, 129–160.

VON KÁRMÁN, T. 1937 The fundamentals of statistical theory of turbulence. *J. Aero. Sci.* **4**, 131–138.

KOLMOGOROV, A. 1941 On the degeneration (decay) of isotropic turbulence in an incompressible viscous fluid. *Dokl. Akad. Nauk SSSR* **31**, 538–540.

KROGSTAD, P.-A. & DAVIDSON, P. A. 2010 Is grid turbulence Saffman turbulence? *J. Fluid Mech.* **642**, 373–394.

LARSSEN, J. V. & DEVENPORT, W. J. 2011 On the generation of large-scale homogeneous turbulence. *Exp. Fluids* **50**, 1207–1223.

LAVOIE, P., DJENIDI, L. & ANTONIA, R. A. 2007 Effects of initial conditions in decaying turbulence generated by passive grids. *J. Fluid Mech.* **585**, 395–420.

LEE, S. K., BENAISSA, A., DJENIDI, L., LAVOIE, P. & ANTONIA, R. A. 2012 Scaling range of velocity and passive scalar spectra in grid turbulence. *Phys. Fluids* **24**, 075101.

LEE, S. K., DJENIDI, L., ANTONIA, R. A. & DANAILA, L. 2014 On the destruction coefficients for slightly heated decaying grid turbulence. *Int. Jnl Heat and Fluid Flow* **43**, 129–136.

LIN, C. C. & REID, W. H. 1963 Turbulent flow, Theoretical aspects. In *Handbuch der Physik* (ed. S. Flugge & C. A. Truesdell), vol. 8, p. 438. Springer.

LING, S. C. & HUANG, T. T. 1970 Decay of weak turbulence. *Phys. Fluids* **13**, 2912–2924.

MANSOUR, N. N., KIM, J. & MOIN, P. 1987 Reynolds-stress and dissipation rate budgets in a turbulent channel flow *NASA Tech. Mem.* 89451.

MANSOUR, N. N. & WRAY, A. A. 1994 Decay of isotropic turbulence at low Reynolds number. *Phys. Fluids* **6**, 808–813.

MELDI, M. & SAGAUT, P. 2013 Further insights into self-similarity and self-preservation in freely decaying isotropic turbulence. *J. Turbul.* **14**, 24–53.

MOHAMED, M. S. & LARUE, L. 1990 The decay power law in grid-generated turbulence. *J. Fluid Mech.* **219**, 195–214.

MYDLARSKY, L. & WARHAFT, Z. 1996 On the onset of high-Reynolds number grid-generated wind tunnel turbulence. *J. Fluid Mech.* **320**, 331–368.

REID, W. H. 1956 On the approach to the final period of decay in isotropic turbulence according to Heisenberg's transfer theory. *Proc. Natl Acad. Sci.* **42**, 559–563.

RISTORCELLI, J. R. & LIVESCU, D. 2004 Decay of isotropic turbulence: fixed points and solutions for nonconstant G R_λ palinstrophy. *Phys. Fluids* **16**, 3487–3490.

RUBINSTEIN, R. & CLARK, T. T. 2005 Self-similar turbulence evolution and the dissipation rate transport equation. *Phys. Fluids* **17**, 095104.

SAFFMAN, P. G. 1967 The large-scale structure of homogeneous turbulence. *J. Fluid Mech.* **27**, 581–593.

SPEZIALE, C. G. & BERNARD, P. 1992 The energy decay in self-preserving isotropic turbulence revisited. *J. Fluid Mech.* **241**, 645–667.

SUCCI, S. 2001 The lattice Boltzmann equation for fluid dynamics and beyond. In *Numerical Mathematics and Scientific Computation*, Oxford University Press.

TAVOULARIS, S., BENNETT, J. C. & CORRSIN, S. 1978 Velocity-derivative skewness in small Reynolds number, nearly isotropic turbulence. *J. Fluid Mech.* **88**, 63–69.

TENNEKES, H. & LUMLEY, J. L. 1974 *First Course in Turbulence*. 3rd edn. MIT Press.

WYNGAARD, J. C. 2010 *Turbulence in the Atmosphere*. Cambridge University Press.

ZHOU, T. & ANTONIA, R. A. 2000 Reynolds number dependence of the small-scale structure of grid turbulence. *J. Fluid Mech.* **406**, 81–107.

ZHOU, T., ANTONIA, R. A. & CHUA, L. P. 2002 Performance of a probe for measuring turbulent energy and temperature dissipation rates. *Exp. Fluids* **33**, 334–345.

ZHOU, T., ANTONIA, R. A., DANAILA, L. & ANSELMET, F. 2000 Transport equations for the mean energy and temperature dissipation rates in grid turbulence. *Exp. Fluids* **28**, 143–151.